Ultrafast single-electron diffraction at 100 keV and investigation of carbon-nanotube dynamics

Daniel Kreier

München 2015

Ultrafast single-electron diffraction at 100 keV and investigation of carbon-nanotube dynamics

Daniel Kreier

Dissertation
an der Fakultät für Physik
der Ludwig–Maximilians–Universität
München

vorgelegt von
Daniel Kreier
aus Schweinfurt

München, den 28. Januar 2015

Erstgutachter: Prof. Dr. Ferenc Krausz

Zweitgutachter: Prof. Dr. Jochen Feldmann

Tag der mündlichen Prüfung: 17. Juni 2015

Zusammenfassung

Zeitaufgelöste Elektronenbeugung ist ein mächtiges Werkzeug, um ultraschnelle strukturelle Dynamik in Materialien und Molekülen sowohl mit atomarer räumlicher als auch zeitlicher Auflösung zu beobachten. Wegen der Coulombabstoßung ist allerdings die Verwendung von nur einem Elektron, oder wenigen Elektronen, pro Puls notwendig, um die kürzesten Pulsdauern zu erreichen. Elektronen haben recht hohe Streuquerschnitte und deshalb braucht man für Experimente in Transmission sehr dünne Proben, die nur wenige Nanometer dick sind; dies verursacht große Schwierigkeiten bei der Probenherstellung. Bisher wurden ultraschnelle Einzel-Elektronen-Beugungsexperimente nur bei einer Elektronenenergie von 30 keV gezeigt; diese Messungen wurden in unserer Gruppe an der „UED1-Beamline“ durchgeführt.

Diese Arbeit stellt unsere Zweite-Generation-Beamline, „UED2“, vor. Die Beschleunigungsspannung der Elektronen wurde hierbei von 30 auf 100 kV erhöht, was die Untersuchung signifikant dickerer Proben ermöglicht. Im Experiment werden Elektronenpulse durch einen Zweiphotonen-Photoprozess erzeugt und die langfristige Stabilität der Quelle wird gezeigt. Die Proben kann man sowohl in Transmission als auch im streifenden Elektronen-Einfall (grazing-incidence) platzieren und um Phase-Matching zwischen den optischen und Elektronenpulsen zu erreichen, können verkippte optische Pulse verwendet werden. Um zeitliche Verzerrungen (Distorsionen) in den verkippten Pulsen zu vermeiden, muss die Geometrie für deren Erzeugung so gewählt werden, dass die Ausbreitungsrichtung der verkippten Pulse senkrecht zur Gitteroberfläche ist. Dass und wie dies möglich ist, wird hier gezeigt. Außerdem werden zeitliche Distorsionen in ultrakurzen Elektronenpulsen, die durch schlecht justierte Magnetlinsen verursacht werden, untersucht. Es zeigt sich, dass eine Verschiebung oder Verkippung der Magnetlinse zu signifikanten zeitlichen Aberrationen im Femtosekundenbereich führt und diese Pulsverlängerungen nur minimiert werden können, wenn der Strahl genau auf der Symmetrieachse der Linse liegt. Ein

hier experimentell gezeigtes Verfahren zum Ausrichten von Linsen-Position und Neigung verringert die Aberrationen auf weniger als eine Femtosekunde.

Für die „UED2-Beamline“ wurde ein neues Labor eingerichtet und ein erstes zeitaufgelöstes Elektronenbeugungs-Experiment an dieser Beamline durchgeführt. Eine anisotrope Bewegung der Atome in Kohlenstoff-Nanoröhrchen wurde beobachtet, welche die Natur der chemischen Bindungen in diesem System widerspiegelt, die zwischen relativen schwachen van der Waals und starken kovalenten Wechselwirkungen variiert.

Insgesamt ist damit gezeigt, dass ultraschnelle zeitaufgelöste Elektronenbeugung bei 100 keV mit einzelnen/wenigen Elektronen pro Puls eine hervorragende Methode darstellt, ultraschnelle atomare Dynamik auch in komplexen Festkörperproben mit höchstmöglicher Auflösung in Raum und Zeit untersuchen zu können.

Abstract

Time-resolved electron diffraction is a powerful tool to observe ultrafast structural dynamics in materials and molecules with atomic spatial as well as temporal resolution. Due to Coulomb repulsion, however, the use of only single-electrons or few-electrons per pulse is inevitable to reach the shortest pulse durations. Electrons have rather high scattering cross sections and thus experiments in transmission require ultrathin samples in the nanometer-range, making sample preparation very challenging. Up to now, ultrafast single-electron diffraction was only demonstrated at an electron energy of 30 keV; these measurements were performed in our group at the "UED1-beamline".

This work introduces our second-generation beamline, "UED2", where the electron acceleration voltage is upgraded from 30 to 100 kV, which allows the investigation of significantly thicker samples. This is decisively widening the range of complex materials that can be studied. In the experiment, electron pulses are generated by a two-photon photoemission process and the long-term stability of the source is shown. The samples can be placed in transmission as well as grazing-incidence geometry. To achieve phase-matching between the optical and electron pulses, tilted optical pulses can be applied. We figured out that to avoid temporal distortions in tilted pulses, a geometry must be chosen in which the propagation direction of the tilted pulses is perpendicular to the grating's surface. Furthermore, temporal distortions for ultrashort electron pulses caused by misaligned magnetic lenses are examined. It is found that a displacement or tilt of the lens causes significant temporal aberrations on a femtosecond time scale and pulse-lengthening is only minimized if the beam travels precisely on the symmetry axis. An experimental procedure detailed here for aligning lens-position and -tilt reduces the aberrations to less than one femtosecond.

For the "UED2-beamline", a new laboratory was established and a first time-resolved electron diffraction experiment at this beamline performed. Anisotropic

ultrafast atomic motion in carbon-nanotubes was observed, revealing the nature of the system's chemical bonds, which vary from relatively weak van der Waals to strong covalent interactions.

In summary, it is thus shown that ultrafast electron diffraction at 100 keV with single/few electrons per pulse is an excellent method to study ultrafast atomic-scale dynamics even in complex solid samples with the highest possible resolution in space and time.

Contents

List of Figures

List of scientific publications

L. Kasmi, D. Kreier, M. Bradler, E. Riedle, and P. Baum. Femtosecond single-electron pulses generated by two-photon photoemission close to the work function. *New J. Phys*, in review, 2015.

D. Kreier, D. Sabonis, and P. Baum. Alignment of magnetic solenoid lenses for minimizing temporal distortions. *Journal of Optics*, 16(7):075201, July 2014.

D. Kreier and P. Baum. Avoiding temporal distortions in tilted pulses. *Optics Letters*, 37(12):2373–2375, June 2012.

Y. E. Romanyuk, D. Kreier, Y. Cui, K. M. Yu, J. W. Ager, and S. R. Leone. Molecular beam epitaxy of InGaN thin films on Si (111): Effect of substrate nitridation. *Thin Solid Films*, 517(24):6512–6515, October 2009.

J. W. Ager, L. A. Reichertz, Y. Cui, Y. E. Romanyuk, D. Kreier, S. R. Leone, K. M. Yu, W. J. Schaff, and W.Walukiewicz. Electrical properties of InGaN-Si heterojunctions. *Phys. Status Solidi C*, 6(S2):S413–S416, June 2009.

1 Introduction

In order to understand many processes in physics, chemistry or biology it is necessary not only to perform static experiments, but also to investigate the temporal dynamics of such systems. The human eye however can only resolve dynamics with a time resolution of about hundred milliseconds [1]. To record faster processes, other measurements techniques had to be developed. One of the first of such experiments was done in 1878 by E. J. Muybridge, who captured the movements of a galloping horse with an arrangement of several glass-plate cameras that were triggered one after another when the horse passed (figure 1.1); with this technique he could achieve a temporal resolution of $\sim 0.04\ s$ [2]. Since then, many scientist steadily improved the time resolution and nowadays photography reaches a temporal resolution down to 10 ps [3].

However, to observe atoms or electrons in motion, one needs femtosecond, respectively attosecond, temporal resolution and also an appropriate spatial resolution. Promising techniques to reach spatial and temporal atomic resolution simultaneously are time-resolved X-ray- or electron-diffraction experiments. With the development of the laser in 1960 [4], the timescale to record atoms or even electrons in motion has today come within reach; pulse durations in the attosecond regime were first demonstrated in 2001 by M. Hentschel et al. [5]. Modern electron and X-ray diffraction apparatuses easily achieve atomic spatial resolution and by the combination with laser-technology the road to make molecular movies is paved [6–8]. In a pump-probe scheme, an ultrashort laser pulse is used to trigger (to pump) the dynamics of interest, and an electron or X-ray pulse, provided at different time delays, records the reactions, whereas the time resolution is only limited by the duration of the two pulses.

Using free-electron lasers (FEL), coherent X-ray pulses with few-femtosecond durations were already successfully demonstrated [9–12] and pulse durations in the attosecond regime were proposed by shaping and compressing the electron bunch [13].

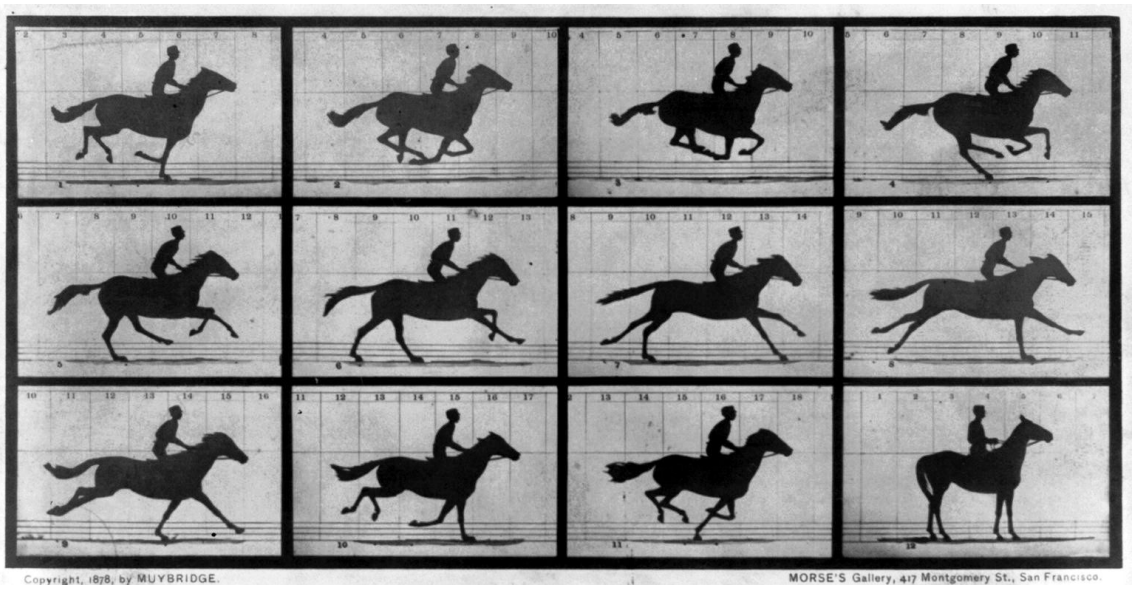

Figure 1.1: The horse in motion, by Eadweard James Muybridge in 1878. To capture the movements of a galloping horse, Muybridge used an arrangement of several glass-plate cameras triggered one after another when the horse passed. The photographs were taken at a distance of about 70 *cm* corresponding to a time interval of about 0.04 *s* [2].

Such sources however require expensive MeV to GeV particle accelerators and are until now available in only a few facilities worldwide. Recent progress in developing table-top laser-driven particle accelerators [14, 15] might improve this situation and maybe make few-femtosecond X-ray pulses in the future available to a broader community [16–18].

Pulsed electron sources, however, are relatively inexpensive, compact and uncomplicated compared to free-electron laser facilities. Another advantage is that electron trajectories are easily controllable by using electro-magnetic fields. Further differences are that electrons have much higher scattering cross-sections and therefore a much smaller penetration depth [19]. The radiation damage threshold is therefore much lower, while ultrashort X-ray pulses typically destroy the sample, allowing often only single-shot experiments [20].

On the downside, electrons are charged particles and due to space charge repel each other, making it hard to achieve ultrashort pulses. To circumvent this problem of Coulomb repulsion, one can use only a single or few electrons per pulse [21, 22]. This, of course, requires long measurement times, a good signal-to-noise ratio and

an efficient long term-stability of the experimental apparatus. Nevertheless, ultrafast pump-probe single-electron diffraction at 30 keV on graphite was recently successfully demonstrated by S. Lahme et al. [23, 24] at our first-generation beamline (UED1) [24, 25]. Another approach to reach shorter pulses is to compress the electron bunch using microwave cavities or pondermotive gratings [26–28]; simulations predict few-femtosecond and even attosecond pulse durations [6, 29, 30]. The shortest electron pulse duration recorded so far was achieved with microwave compression of single-electron pulses and is about 28 fs (FWHM) [31, 32].

Figure 1.2 shows the schematic of a typical ultrafast electron diffraction (UED) experiment. An ultrashort laser pulse is split into two beams by a beam splitter (BS). One pulse, the so-called pump pulse, is focused by a lens (FL) onto the sample and triggers the dynamics of interest. The other pulse, the probe pulse, is send to a photo-emission electron source to generate electron pulses. In a static electric field the electrons are accelerated and focused by electron optics to the sample (here the case of transmission geometry is shown). Finally, a detector records the diffraction patterns. By varying the delay between pump and probe pulse, one can record dynamics with atomic resolution in space and time.

Suitable electron energies for ultrafast electron diffraction are in the range of $30 - 300\ keV$, corresponding to a de Broglie wavelength of $2 - 7\ pm$ and therefore ideal to resolve atomic distances [33]. Because of the electron's relatively large scattering cross-section [19], samples measured in transmission geometry have to be ultrathin or the use of gracing incidence is required. Electrons with an energy of 30 keV have e.g. an attenuation length of about 35 monolayers (figure 2.8 in [34], linearly extrapolated); in metals a monolayer has a thickness of approximately $0.2 - 0.25\ nm$ [34]. Sample preparation is hence very challenging and the use of higher acceleration voltages would strongly benefit this issue.

This work introduces our second-generation beamline, UED2, with acceleration voltages up to 100 kV. The sample can be placed in transmission as well as grazing incidence geometry and to achieve phase matching appropriate tilted optical pulses can be applied. Furthermore results on temporal distortions caused by misaligned magnetic lenses are presented and an alignment procedure to minimize the aberrations to less than one femtosecond is shown. We demonstrate the apparatus's long-term stability, and its feasibility for ultrafast single-electron diffraction using thick samples of a complex material, a foam made of carbon nanotubes. The re-

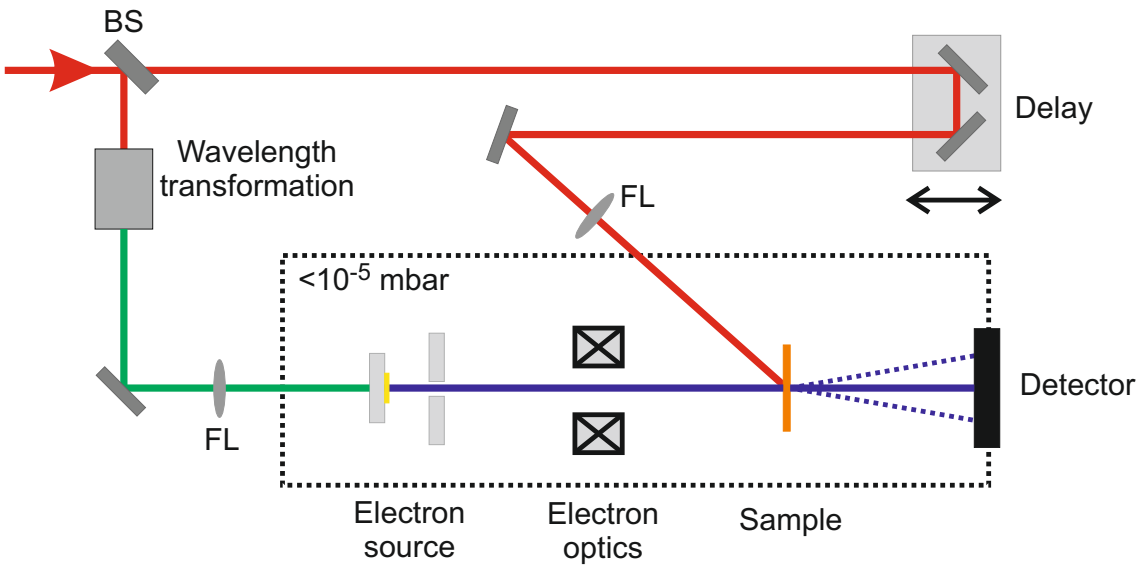

Figure 1.2: Schematic for a typical time-resolved electron diffraction experiment. A laser pulse is split by a beam splitter (BS) into two beams, the so called pump and probe beam. The pump beam is used to excite the sample, while the probe beam is send to a photo-emission electron source to generate electron pulses. This electron pulses are now focused by electron optics to the sample and a detector records the diffraction patterns. By varying the delay between pump and probe pulse, one can record dynamics with atomic resolution.

sults are very promising, and when our apparatus will be combined with available pulse compression techniques, few-femtosecond or even attosecond ultrafast electron diffraction will come in range, at electron energies capable of penetrating a large variety of complex materials, potentially opening up a new era of investigating structural dynamics.

2 Setup of the experimental environment and infrastructure

2.1 New laboratory

For the time-resolved 100-keV ultrafast electron diffraction (UED2) beamline a new laboratory had to be built. This was accomplished within the scope of the renovation of the LMU-building (Am Coulombwall 1, Garching). Prior the space was used for several offices, then the walls were removed and our new laboratory with two anterooms established. Figure 2.1 shows a layout of this new laboratory (E01) and fig 2.2 some pictures taken during the renovation.

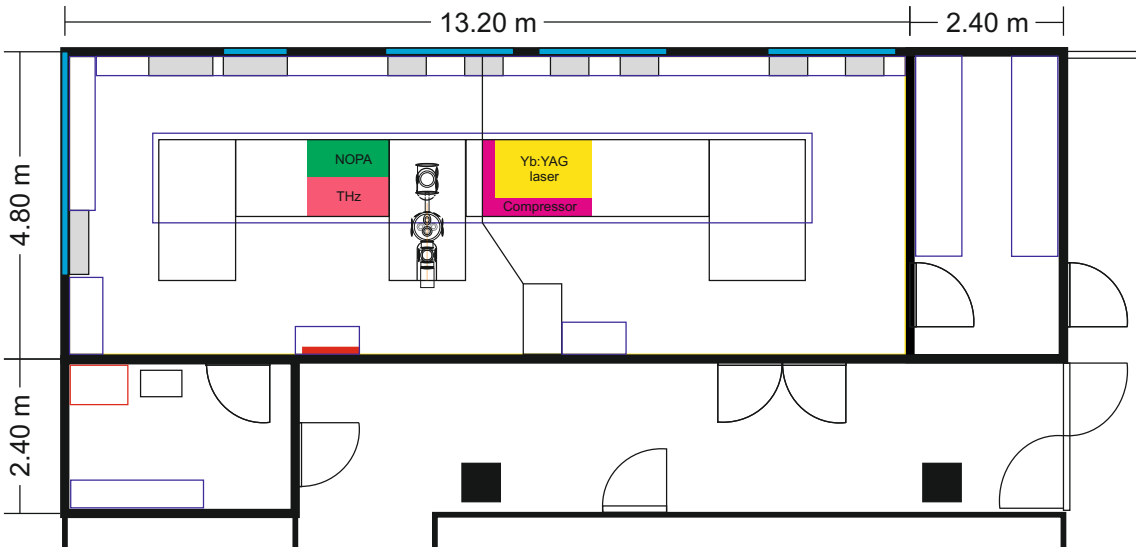

Figure 2.1: Layout of the new laboratory E01 and its anterooms. The optical tables and the key-elements of the time-resolved electron diffraction experiment are also illustrated.

Figure 2.2: Pictures of the new laboratory that was built for the 100 keV electron diffraction experiment. The first picture was taken in July 2011 and shows only a construction area; in February 2012 the optical tables arrived and in September 2013 the first diffraction measurements were made.

In practice, you enter the laboratory through one of the anterooms (E01a or E05), where you change shoes and put on a laboratory-coat and hairnet to avoid bringing dirt into the laboratory-environment. Almost all chillers and the vacuum pre-pumps are located in the two anterooms, in order to eliminate unwanted fluctuating heat sources, noise and vibrations in the main laboratory. The main laboratory is divided into two parts: the laser development and the electron diffraction site. The two parts can be separated by flexible laser safety walls, so that one can work without safety goggles on the electron diffraction site if no high-intensity laser beam is needed there. Above the optical tables, a hanging rack is installed that holds several flow-boxes providing a continuous flow of clean air to avoid any dust on the optics. Moreover, in the laser development area, side walls are attached to the hanging rack so that the laser systems can be completely covered.

For ultrafast pump probe experiments it is essential to provide a very stable room-temperature in order to prevent movements caused by heat expansion. For example for laser pulses, a mirror's displacement of $\Delta s = 10\ \mu m$ causes a timing change of $\Delta t \approx 66\ fs$. Figure 2.3 shows the temperature stability in our laboratory during a pump probe experiment that lasts $\sim 47\ h$. In the laser housing we reach a temperature stability better then 90 mK peak to peak and with a standard deviation of $\sigma = 14.84\ mK$. Near the electron beam line we measured fluctuations of $\sigma = 45.52\ mK$; the fluctuations are higher because the diffraction experiment is not covered like the laser, but the stability is well sufficient for our experiments.

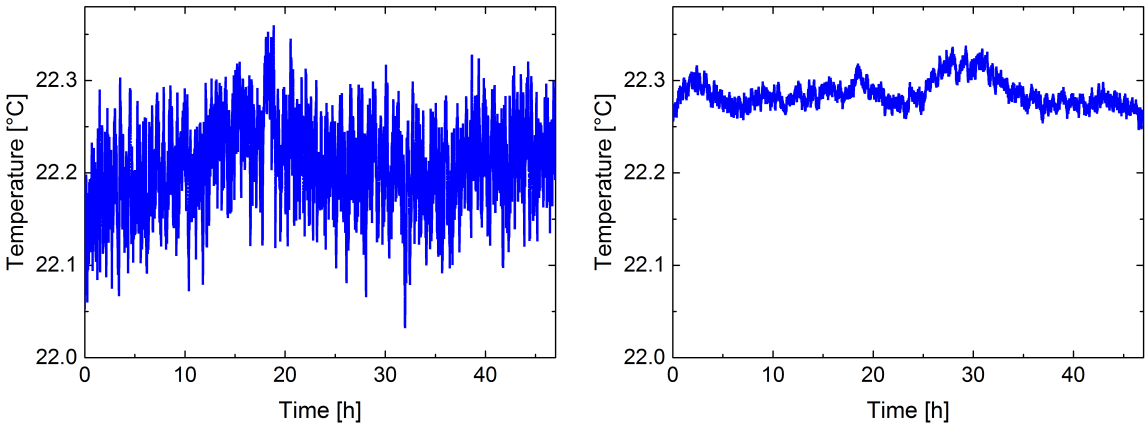

(a) Temperature near the electron beam line **(b)** Temperature in laser housing

Figure 2.3: (a) Temperature stability near the electron beam line and (b) in the laser housing during a pump probe experiment. The fluctuations near the laser are less then 90 mK peak to peak and the standard deviation is $\sigma = 14.84\ mK$; near the electron beam line $\sigma = 45.52\ mK$.

Since we are dealing with charged-particle beams, it is crucial to provide not only a very stable room temperature but also a stable magnetic-field environment. If the magnetic field is changing during a laser-pump electron-probe experiment, the electron beam can be deflected and you will loose the spatial overlap. A change in the magnetic field of $\sim 40\ nT$ measured on top of the sample chamber, displaces our electron beam by 1 *pixel* ($\sim 15.6\ \mu m$) on the detector. The use of non-magnetic materials near the electron beam line and placing potential sources of changing magnetic fields as far away as possible helps to suppress such fluctuations. But fluctuations coming from outside the laboratory-environment are not so easy to

handle. In our case the main contribution of changing magnetic fields outside the laboratory comes from an elevator and a power cable running in the basement. To compensate such fields, the electron beamline is placed in the volume of three large solenoid pairs around the whole experiment, generating an appropriate opposing magnetic field via feedback electronics, if required. Such magnetic-field stabilization systems are commercially available (Magnetfeldkompensationsanlage Macom II, Müller BBM GmbH) and widely used in electron microscopy [24, 35].

2.2 Laser system at 50-400 kHz

The laser system used for the UED2 beamline is a home-built Yb:YAG thin-disk laser and is mainly described by Schneider et al. in [36]. It delivers $\sim$ 800-fs pulses with an average output power of up to 100 W at a central wavelength of 1030 nm. Figure 2.4(a) shows the output spectrum and 2.4(b) an autocorrelation trace, fitted assuming a sech^2-shaped temporal pulse profile [36]. The repetition rate of the laser can be tuned between 50 and 400 kHz, ideal for ultrafast electron diffraction experiments [23]. The output is also sufficiently intense for many applications like nonlinear optical frequency conversions (e.g. the NOPA-system described in chapter 3.5) and THz generation [36] that can be used to excite the desired atomic-scale dynamics.

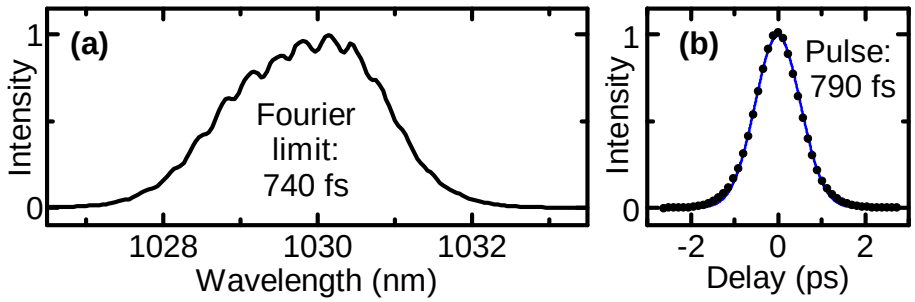

Figure 2.4: Laser performance in the time-bandwidth domain, taken from [36]. (a) Output spectrum; (b) autocorrelation trace and fit, assuming a sech^2-shaped temporal pulse profile.

Because of the long optical beam path from the laser to the electron diffraction site (cf. chapter 2.1), a beam-stabilization system (Aligna 4D, TEM Messtechnik GmbH) is used to deliver the laser pulses to the electron diffraction apparatus.

3 Time-resolved electron diffraction setup at 100 keV

This chapter deals with the time-resolved electron diffraction setup that was built in the new laboratory. The electron diffraction apparatus consist mainly of four parts, the electron source where the pulsed electron beam is generated, the electron optics to focus and/or steer the beam, the sample chamber where the dynamics you want to study takes place, and the detector that records the diffraction images.

The electron source, the electron beamline and the detector is placed in a ultrahigh vacuum chamber system that can reach pressures down to 10^{-9} $mbar$. A low pressure is beneficial for such experiments because the number of residual gas molecules is reduced and therefore scattering of the electrons is eliminated. It is also important that surface-contamination of the photocathode and the sample is avoided. Contamination of the photocathode will affect the long-term stability [24] and can reduce the breakdown voltage of the electron source by as much as 50 % [37], while contamination of the sample is bad for surface-sensitive measurements or bulk samples with a large surface area, such as the carbon-nanotubes described in chapter 4.

Figure 3.1 shows a top-view of the electron beamline. The core assembly is firmly attached to the optical table to prevent mechanical instabilities and drifts. Supporting systems, i.e. the vacuum pumps are separated by flexible spring bellows to avoid transfer of any vibrations to the main experiment. The pumping system is located on the floor below the optical table and consists of two ion-getter pumps (600L-CV-8S-SC-220-N, VACOM Vakuum Komponenten und Messtechnik GmbH) and two turbomolecular pumps (HiPace 700, Pfeiffer Vacuum GmbH) which are pre-pumped by a scroll pump (Scrollvac SC15D, Oerlikon Leybold Vacuum GmbH). The electron source chamber, the sample chamber and the detector are separated by valves and can thus be vented individually to atmosphere or Argon gas. The

vacuum chambers as well as the optical table are made from materials with lowest magnetic permeability, such as Titanium and "A4" stainless steel (1.4404 or 1.4429ESU). As mentioned earlier (2.1), it is important to avoid varying magnetic fields near the electron beamline. The ion-getter pumps have no such influence on the beam, because their magnetic fields are static and they are placed far enough away.

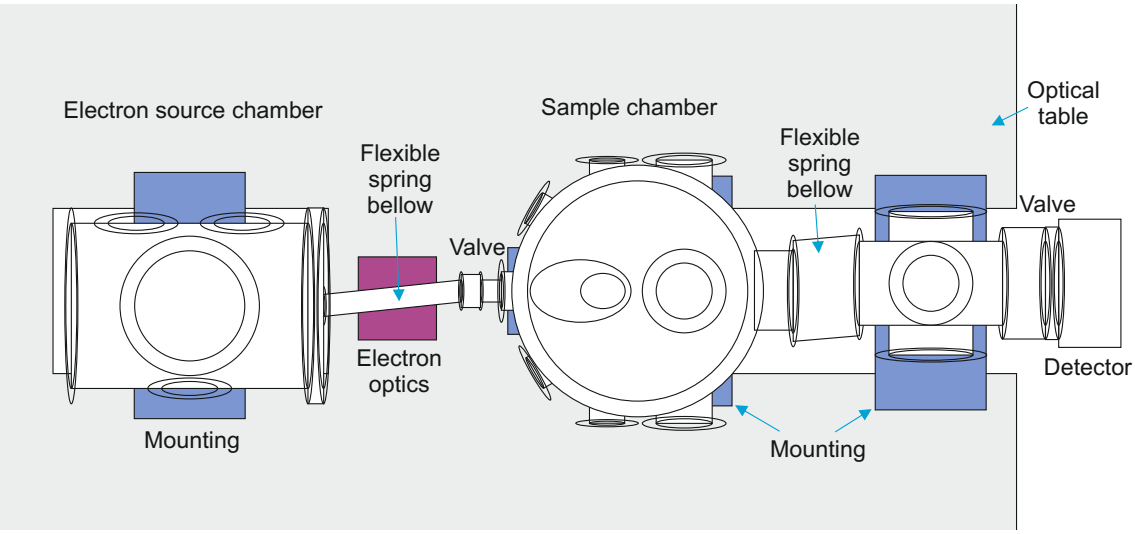

Figure 3.1: Beamline of the time-resolved electron diffraction setup (top-view). The total length of the vacuum beamline is roughly 1.8 m. The individual chambers are not arranged in a straight line with respect to the electron source, because the electrons are slightly deflected in the earth magnetic field. The gray area depicts the optical table.

One significant magnetic field, however, can not be avoided; this is the magnetic field of the earth. The vertical strength of the earth magnetic field in Garching equals $B \approx 43.4\ \mu T$ [38]. Figure 3.2 shows a simulation of the lateral deflection of electrons that travel in such a magnetic field. In our case, the path length from the photocathode to the detector equals 1.42 m; therefore electrons with an energy of 100 keV are 4.2 cm laterally displaced at the position of the detector. This displacement with respect to the electron source was taken into account by proper arrangement of the chambers along a slightly curved path.

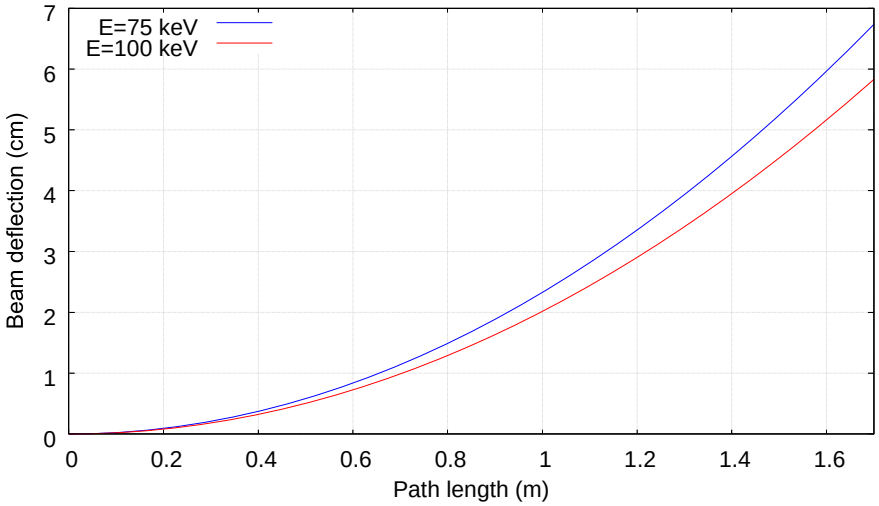

Figure 3.2: Lateral deflection of an electron beam in the earth magnetic field in Garching for electrons with energies of 75 keV and 100 keV, respectively.

3.1 Single-electron source at 100 keV

As discussed earlier (chapter 1), a huge improvement compared to the first-generation single-electron diffraction apparatus (UED1) in the group of Baum and Krausz (described mainly by Friedrich Kirchner [25] and Stefan Lahme [24]) is the significantly higher acceleration voltage in the electron source here. This section describes the electron source design from the high-voltage point of view, while in section 3.5 the generation of shortest and most stable electron pulses is addressed.

The 100-keV single-electron source was built with help of the mechanical workshop. Figure 3.3 shows a overview of the electron gun. The assembly consists of three aluminum parts, the grounded mounting ring, the -100 kV high-voltage pot with the gold-coated photocathode and the grounded anode element with the anode hole. These three parts are electrically separated from each other by insulating polyimide posts.

For the design of the electron source some high-voltage considerations have to be taken into account. First of all you only want to have a high acceleration field between the cathode and the anode, but the field must be well below the electrical breakdown limit of vacuum. If the electric field at some local point (also called the hot spot [37]) is too high, arcing will occur. Electrons are emitted from the surface, accelerated to a grounded part and at a sufficiently high energy positive

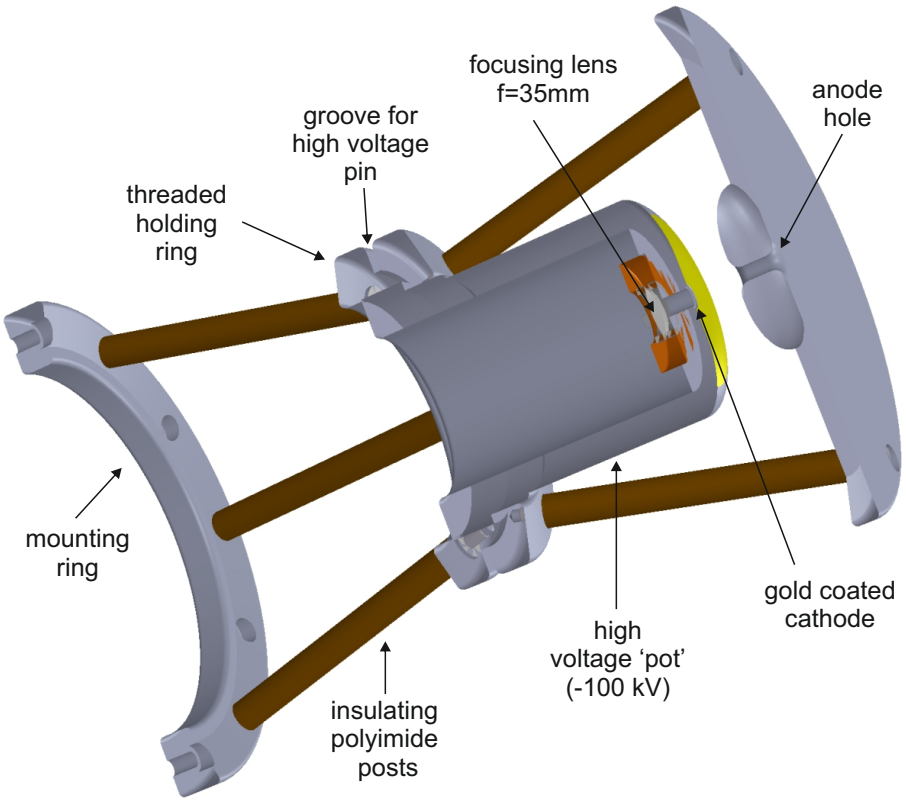

Figure 3.3: Design of the 100-keV electron source. Electrons are generated by femtosecond photoemission at the gold coated photocathode and then accelerated towards the grounded anode. For further details, see the text.

ions are their released [39]. The ions are flying back to the hot spot and increase the emission of electrons. An avalanche effect occurs, leading eventually to breakdown. The voltage applied to the high-voltage pot drops and a current is flowing through the generated conducting path. By monitoring the applied voltage, current and pressure you have a experimental feedback. It is also important that you design a good grounding concept, so that in case of a breakdown, most of the energy is discharged through a well-grounded cable; if not, this can severely damage other laboratory-equipment. The breakdown limit depends on the pressure p and the distance d between the high-voltage part and a grounded surface, which is described by Paschen's law [40]. For low pressures in the high-vacuum regime the breakdown limit for a distance $d = 25\ mm$ was experimentally determined to 16 kV/mm [37]. Note that this experiments were done under perfect conditions with very clean and

microscopically flat surfaces. In our case we have a acceleration field of $\sim 4\ kV/mm$ that is well below this limit.

If the metal-surfaces in the electron source are not flat but curved, the conditions change dramatically. Sharp edges or whiskers lead to field enhancement and field emission can already occur at much lower voltages. Because of the locally high field strength, the whiskers are heating up and can evaporate. The pressure will rise and the probability that the residual gas gets ionized is increased. Therefore clean and microscopically flat surfaces are desired for such high-voltage applications.

Furthermore, a current can flow along the surface of insulators, a breakdown called surface flashover [41]. Surface flashover of insulators is initiated by the emission of electrons from a triple junction, i.e. the point where metal, insulator, and vacuum meet. Electrons travel on the insulator surface, causing desorption of gas that has been adsorbed. The gas is ionized, finally leading to surface flashover. Especially when the electric field lines are parallel to the insulator surface, the emitted electrons can gain a high enough energy to cause flashover [20, 42]. In [42], it is claimed that a gradient of $\leq 3\ kV/cm$ parallel to insulator surfaces is sufficient to avoid such breakdowns.

To fulfill these high-voltage requirements, we designed the 100-keV electron-source with COMSOL-Multiphysics, a simulation tool that is based on the finite-element-method. Fig. 3.4 shows the electric field of the resulting optimized geometry in the cathode-anode region (two-dimensional cut). Electrons are generated at the cathode (position 0/0) by photoemission and accelerated on the symmetry axis to the anode hole. The shape of the anode/cathode is the result of a trade-off between a high acceleration field on the symmetry axis and a safe distance and safe degree of curvature to prevent electrical breakdown. The distance between the cathode and anode is set to $d = 25\ mm$, resulting in an acceleration field of $E_{acc} \approx 4\ kV/mm$ for a potential difference of $\Delta V = 100\ kV$ as shown in figure 3.5. According to particle tracking simulations, an anode hole diameter of 8 mm is large enough for the entire electron beam to exit the electron source; this is important in the single-electron regime [43].

All metal surfaces in the electron source are mechanically and electro-chemically polished to provide smooth surfaces. The metal parts are made of aluminum. Aluminum is normally not the first choice for high voltage applications because its surface is rapidly attacked by oxygen that results in an insulating oxide layer [44].

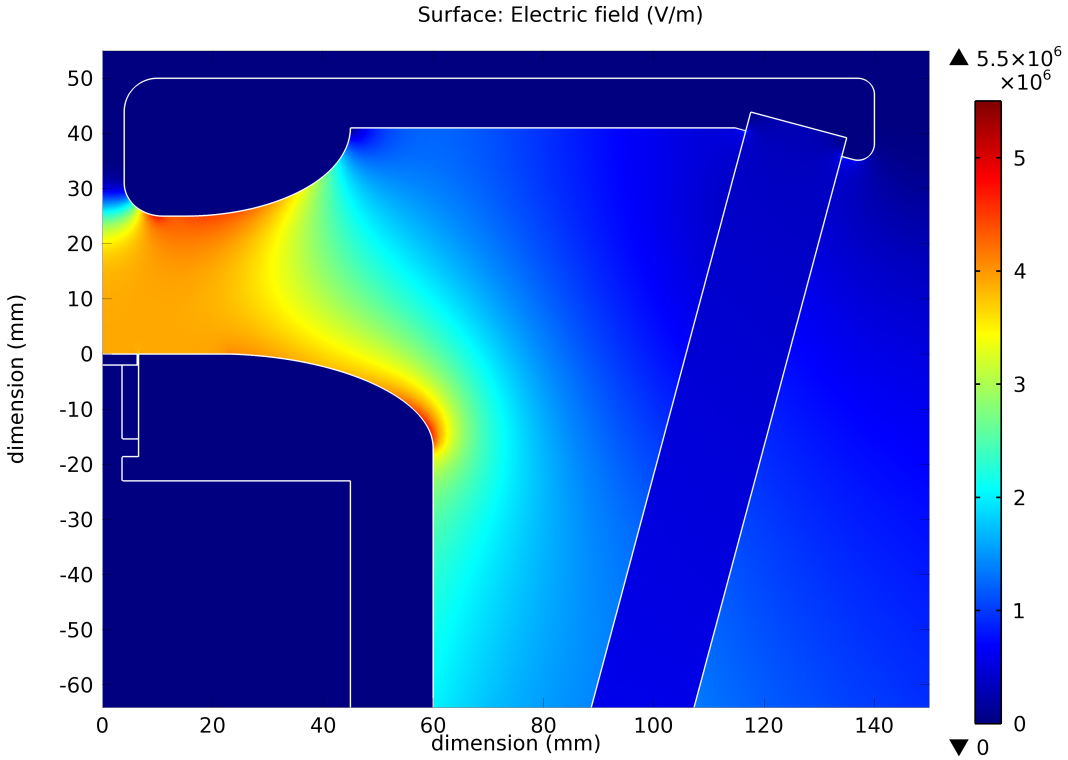

Figure 3.4: Dimensions and electric field in the cathode-anode region. The potential difference between the anode and cathode is set to $\Delta V = 100\ kV$. The electric field distribution was calculated with Comsol-Multiphysics. For further details, see text.

Nevertheless we chose aluminum because it is easy to machine and has a low weight compared to, e.g., copper. In our design of the electron source, copper would have been too heavy to be supported by the insulating posts. To overcome the problem of oxidation, the surface of the high voltage pot facing the anode disk is coated with a gold layer.

The insulating post separating the high voltage parts are made of Tecasint 2011, a polyimide material from the company Ensinger Sintimid. It has a sufficiently high dielectric strength of $D = 21.8\ kV/mm$ [45]. The posts have a length of 178.5 mm and are oriented such that the electric field lines are not parallel to their surface.

The substrate for the photocathode itself is a transparent 1-mm thick sapphire plate with a diameter of 12.7 mm. The substrate fits tightly in a clearance in the high voltage pot and is fixed with very little amount of silver paste. The high voltage pot together with the sapphire substrate is then coated with a 20 nm gold layer.

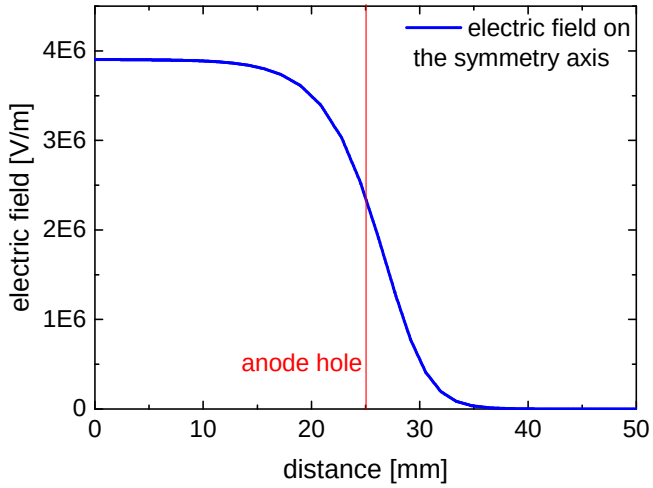

Figure 3.5: Electric field on the symmetry axis of the electron source. The position of the cathode is at 0 mm, the anode hole at 25 mm. The potential difference ΔV between the cathode and anode is set to $\Delta V = 100\ kV$.

The coating of the entire cathode surface facing the anode disk provides a very smooth surface avoiding any inhomogeneities at the point where the sapphire meets the aluminum surface. Furthermore you avoid the problem of electrically connecting the thin 20-nm layer on the sapphire to the high voltage.

The high-voltage pot is screwed in a holding ring (see Fig. 3.3) and can be taken out of the vacuum system by only opening a single CF160 flange. With a specially designed mechanical tool it can be removed conveniently so that it is not necessary to dismantle the electron source completely for exchanging the photocathode. By having a second high-voltage pot with a photocathode prepared, you can exchange them pretty fast, reducing service time from hours to minutes. The whole electron source is mounted on a CF300 flange and can also be accessed easily with accordant mechanics. Figure 3.6 shows a picture of the mounted electron source ready to be put into the vacuum chamber.

The high-voltage pot is connected to a high-precision high-voltage power supply (PNChp+150000-1neg, Heinzinger electronic GmbH) having an output ranging from 0 to $-150\ kV$ with a stability $\leq 0.0005\% V_{nom}$ [46] and a maximum current of 1 mA. The high-voltage coaxial cable (HVC150 2121, Essex) enters the electron-source vacuum chamber via a feedthrough that was designed together with the company

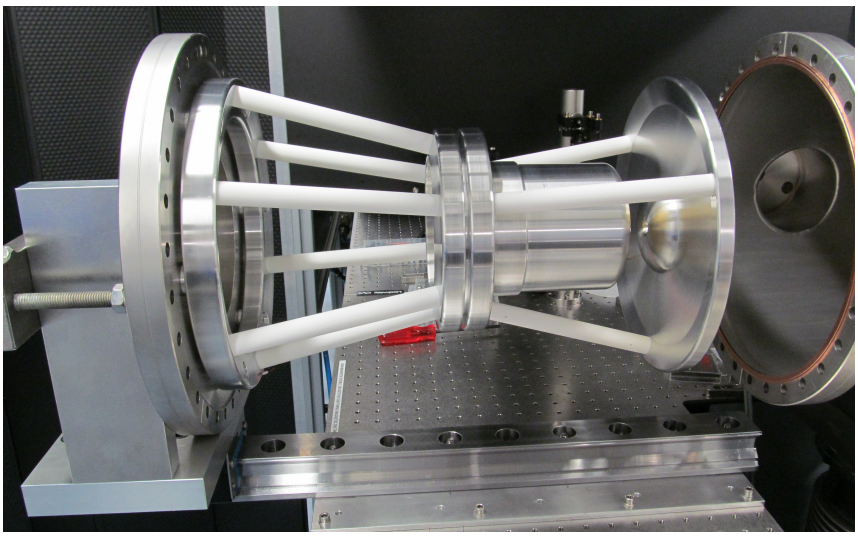

Figure 3.6: Picture of the mounted electron source ready to put in the vacuum chamber.

Friatec. The feedthrough is electrically insulated by a ceramic (Frialit F99,7) with a total length of 530 mm (284 mm on the vacuum side and accordingly 246 mm outside the vacuum chamber) which is sufficient enough to avoid breakdown.

Even with polished metal surfaces it is not possible to apply the $-100\ kV$ to the electron source by just turning a switch. You have to carefully remove remaining whiskers by controlled breakdowns. This is called conditioning of the electron source. The voltage is gradually ramped until a breakdown occurs, then quickly lowered and slowly increased again. With this method, whiskers are evaporated in a controlled way due to heating and the surface gets gradually smoothed. It is crucial that the voltage is lowered in case of a breakdown so that no conduction path can build up that would increase the surface roughness. For a new cathode, the conditioning to $-100\ kV$ takes typically 2 $days$.

3.2 Electron detector

For the detection of electrons, a CMOS camera (TVIPS TemCam-F416 special camera system, Tietz Video and Image Processing Systems GmbH) based on a fiber-optically coupled special low electron energy scintillator is used. The camera has a 64 $mm \times 64\ mm$ field of view with a resolution of $4096 \times 4096\ pixels$. The corre-

sponding pixel size is 15.6 $\mu m \times 15.6$ μm and each pixel is read out with a 16-bit dynamic range [47]. The detector is sensitive to single electrons and can be cooled to 273 K to reduce thermal noise. The exposure time of the camera can be set from 100 ms to 30 s.

A single electron which impinges on the scintillator generates there a certain number of photons, of which a portion is passed through the fiber to the CMOS chip. The chip provides for each pixel a photodiode connected to a capacitor that is charged to a bias at the beginning of the exposure. During exposure, the capacitor is then discharged by a certain amount depending on the incident photon flux [24, 48]. After the image acquisition, all capacitor voltages are read out, resulting in a number of intensity-counts for each pixel. Due to reading out an entire row of pixels simultaneously [49], the readout time of the whole chip lasts only 0.9 s [47].

For a single-electron diffraction experiment it is important to know how much total intensity-counts one electron gives. This has to be determined experimentally. The detected intensity I is given by

$$I(E) = \alpha(E) \cdot N, \tag{3.1}$$

where N is the number of incident electrons per exposure time and α is a sensitivity function that depends on the electron energy. Electrons with higher energy are generating more photons at the scintillator. So it is necessary to identify α for all desired acceleration voltages.

Therefore we recorded the not-diffracted unfocused electron beam at different energies. To detect single electrons independently from each other, you have to set the intensity of the beam very low so that electrons do not overlap on the screen. Figure 3.7(a) shows such a recorded image section. The image is background- and flatfield-corrected. A detailed discussion about the noise of the camera and the correction can be found in [24, 48]. For the evaluation of α we recorded 50 such pictures with a 1-s exposure time for each acceleration voltage and counted for every picture the camera counts caused by a single electron. Since an electron generates several photons at the scintillator that are emitted into all directions, a single electron will not only illuminate one but multiple pixels. This count distribution across adjoining pixels is called point spread function (PSF) of the detector [25]. For this camera system, this width was determined by Kirchner to $\sigma_{PSF} = 0.806 \pm 0.004$ $pixels$ [25]

(standard deviation). Hence we evaluated not only one pixel per electron but a area with at least a side length of $6\sigma_{PSF}$ around the brightest pixels (see Fig. 3.7(b)). To separate real electron counts from noise and defect pixels we only evaluated areas where at least 3 neighboring pixels reach a threshold of

$$I_{th} = 3\sqrt{\sigma_t^2 + \sigma_r^2} \approx 15 \; counts. \tag{3.2}$$

$\sigma_t = (4.4 \pm 0.8)$ *counts* is the width of the thermal noise and $\sigma_r = (0.8 \pm 0.2)$ *counts* the width of the read-out noise. This values were determined by Urban [48].

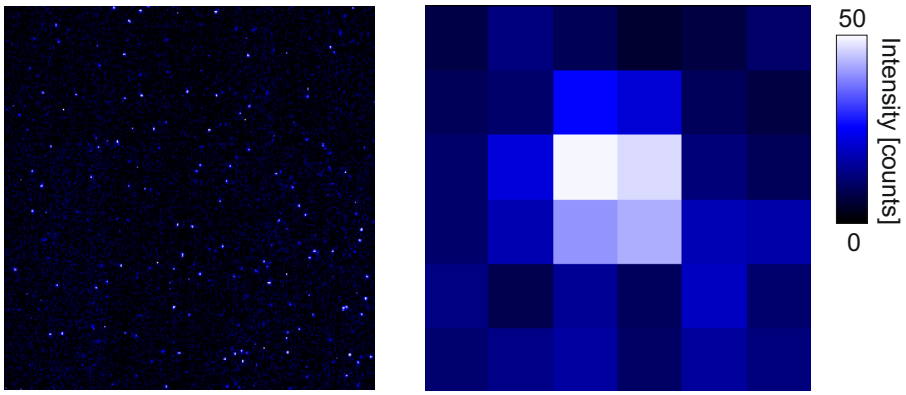

(a) Image section 300 x 300 pixels (b) Image section 6 x 6 pixels

Figure 3.7: (a) Camera image section to measure the intensity-counts one single electron causes. The intensity of the beam is set very low so that the electrons do not overlap on the screen. The electron energy in this case was 100 keV and the exposure time of the camera 1 s. (b) Pixel area that achieves the requirements for the evaluation.

From all areas that achieve those requirements on all 50 pictures the integrated intensity is then calculated. Then we changed the acceleration voltage, set the intensity accordingly that electrons do not overlap on the screen and repeated the procedure.

Unfortunately it was only possible to measure the counts per electron with this method above an electron energy of 70 keV. For lower energies the single-electrons did not provide enough counts to separate them reasonable from the background noise. To measure the counts per electron below 70 keV we generated an electron beam with a constant number of electrons and recorded for different acceleration voltages the intensity on the screen. With equation 3.1 now each intensity is con-

verted to counts per electron. This measurement was done together with bachelor student Theresia Urban. You will find a further discussion also in her thesis [48].

Fig. 3.8 shows the combined results, for electron energies ranging from 35 keV to 100 keV. The curve is not linear with the electron energy but seems to saturate at higher acceleration voltages. This non-linearity comes mainly from the non-proportional response of the scintillator and is heavily discussed in the literature [50–52]. For the here conducted diffraction experiments, it is sufficient to know that a significant amount of digital counts is generated per electron at all relevant energies. The detector's quantum efficiency is close to 100%.

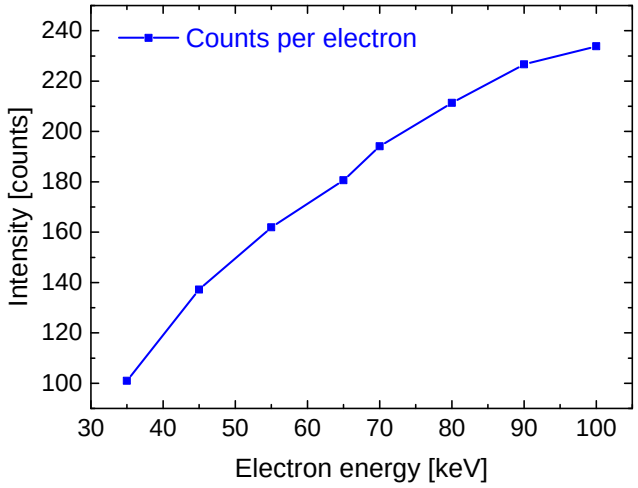

Figure 3.8: Measured intensity-counts a single-electron causes at different electron energies at a exposure time of 1 s.

3.3 Magnetic lenses for steering and focusing the electron beam

Due to the divergence of the electron beam, the beam-size on the sample equals several millimeters and is therefore not suitable for electron diffraction. In order to reach a good spatial resolution, the beam has to be focused. The focusing of charged particle beams at non-relativistic energies is commonly achieved by using magnetic solenoid lenses.

A charged particle interacts with the magnetic field B of the solenoid through the Lorentz force

$$\vec{F} = q(\vec{v} \times \vec{B}), \tag{3.3}$$

with $\vec{v}$ the velocity and q the charge of the particle. Electrons traveling on the symmetry axis will not feel any field, but electrons traveling off axis are forced on a helical path around the axis. Those electrons are accelerated towards the symmetry axis, causing the desired focusing effect [53]. The focal length f for a solenoid lens (with $l \ll f$) is [53, 54]

$$f \approx \frac{4}{\int dz (qB_z/mv_z)^2} \approx \frac{8mU}{q \int B_z^2 dz}, \tag{3.4}$$

with m the particle's mass, v_z the particle's longitudinal velocity and U the kinetic energy. B_z is the longitudinal magnetic field on the symmetry axis and is directly proportional to the number of windings N and the current I flowing through them [55]. The focal length f depends therefore on the acceleration voltage and the coil current I and can thus easily be tuned by changing I.

To focus the 100-keV electron beam, a solenoid (AccTec BV) with 353 windings is used; the inner diameter equals 85 mm and the length is 60 mm. In contrast to the UED1 experiment [24, 25], we decided to place the lens outside of the vacuum system. This allows a much easier design of the required water cooling for heat removal and mechanically more stable holders can be constructed. For avoiding any inhomogeneities in the magnetic field, the vacuum tube inside the solenoid is made of Titanium. To focus electrons with an energy of 100 keV onto the sample, a current of $I = 6.53\ A$ has to be applied (distance middle of the lens-sample $\sim 570\ mm$); assuming that the magnetic field outside the lens disappears quickly, this gives a magnetic field in the lens of about $B_z \approx 12\ mT$ (cf. equation 3.4). The power in the lens equals roughly 34 W.

Furthermore the electron optics setup consists of a pair of deflection coils placed several cm away from the focusing solenoid (see fig. 3.9). This allows to steer the electron beam both horizontally and vertically over the whole range of the electron detector, which can be useful during alignment. We note, however, that for reaching the shortest electron pulse durations the use of such deflection coils shall be avoided,

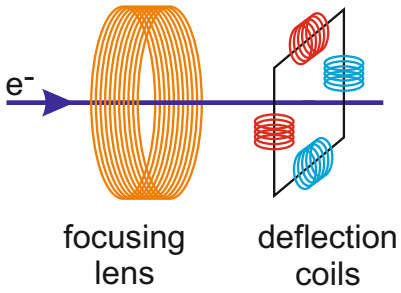

Figure 3.9: Electron optics setup. The electron beam can be focused by a solenoid magnetic lens and steered with two deflection coils. The electron optics are placed outside the vacuum system and can be aligned independently.

because they can produce temporal distortions (see chapter 3.4) and can also change the beam profile.

The solenoid as well as the deflection coils are mounted on flexible post that can be adjusted in all directions (tilt and displacement). This is very important for alignment; see chapter 3.4. The constant current for the coils is provided by stabilized power supplies (PSM-2010, GWInstek).

3.4 Alignment of magnetic solenoid lenses for minimizing temporal distortions

This chapter is also published in Journal of Optics, Vol. 16, No. 7, June 11, 2014 [56]. I specially want to thank Deividas Sabonis from the Department of Quantum Electronics at the Vilnius University in Lithuania, who was a summer student at this time and helping with the experiments.

Abstract: An ubiquitous focusing element for charged particles is the magnetic solenoid lens. For the case of ultrashort electron pulses, we show here that misalignment of the lens, i.e. displacement or tilt, causes significant temporal aberrations on a femtosecond time scale. Pulse-lengthening is only minimized if the beam travels on the symmetry axis. We present an experimental procedure with periodic reversal of the magnetic field for aligning position and tilt with sufficient precision for reducing the aberrations to less than one femtosecond. This method will be instrumental for

advancing ultrafast electron microscopy and diffraction to ultimate temporal resolutions.

The guiding of charged particles in electron microscopes, diffraction apparatuses, focused ion beams, storage rings, or accelerators is largely based on solenoid lenses, or more generally, inhomogeneous magnetic fields with a radial symmetry. In these devices, the beam travels along the symmetry axis and focusing is caused by the Lorenz force that charged particles feel in the inhomogeneous fields. Besides focusing, this mechanism is typically accompanied by a rotation of the beam around the symmetry axis.

In electron microscopy, spherical and chromatic aberrations are among the most essential effects limiting the spatial resolution, and a lot of effort is made to minimize or compensate these lens distortions [57]. The recent advance of electron microscopy and diffraction to the femtosecond domain [58, 59] makes it necessary to consider also the temporal aberrations of the imaging system. An earlier report from our laboratory [60] indicated that femtosecond electron pulses can lengthen significantly in time when passing through a solenoid lens. It was found that the effective distortions can amount to tens or hundreds of femtoseconds, depending on the focal distance, beam size and divergence. An "isochronic" magnification condition was identified that produces the shortest possible electron pulses at a practical distance for diffraction or microscopy [60].

Here we consider an additional type of temporal distortion, namely imperfections of the lens alignment. The experimental setup is shown in figure 3.10. The typical electron source in pump-probe diffraction and ultrafast microscopy consists of a photoelectric emitter pumped by a focused femtosecond laser. The emitter can be a thin metal layer [61] like in the experiments reported here, or alternatively an LaB6 cathode [58], a cold gas [62–64] or a sharp metallic tip [65, 66]. In all cases, acceleration to energies of typically $30 - 300\ keV$, which provides a suitable de Broglie wavelength for diffraction or microscopy, is achieved with electrostatic fields.

Generally, the electron beam of such sources is divergent: First, the photoelectrons have some initial transverse velocity spread, second, the anode hole or other field inhomogeneities act as an electrostatic lens that is typically defocusing, and

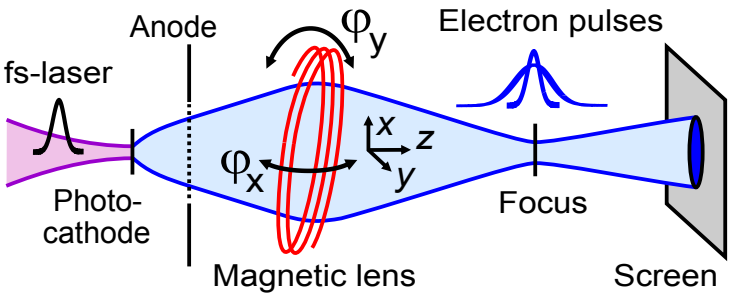

Figure 3.10: A femtosecond laser (violet) impinges on a photocathode (black) and creates a beam of femtosecond electron pulses (blue). Focusing with a misaligned solenoid lens (red) causes temporal aberrations of the electron pulse shape at the focus.

third, multiple electrons repel each other, causing temporal and lateral dispersion by space charge forces (Boersch effect). In 4D microscopy [67] and single-electron diffraction [21], only one or a few electrons are generated at a time [33]. Space charge becomes irrelevant, but the statistics of photoemission and electrostatic effects nevertheless produce a divergent beam and pulses of ultrashort but finite duration [21]. Pulses that are shorter than the duration of photoemission [26] can be generated using time-dependent compression in microwave fields [28] or light gratings [6]. Electron pulses in the few-femtosecond regime are predicted with simulations and first steps have been undertaken [26]; experimental characterization and pulse length measurement is achievable using field-induced streaking with laser pulses [68].

When few-femtosecond or even shorter electron pulses will eventually be achieved in practice, beam transport, focusing and imaging should not distort these ultrashort pulse durations. At least one and typically several solenoid lenses are unavoidable for time-resolved electron microscopy or diffraction for beam collimation and imaging. In practice, it is not typically controlled that the rotational symmetry axis of the magnetic field coincides well with the pulsed electron beam. Sometimes, a displacement of the magnetic lens is used on purpose to steer the electron beam in space. While these residual or intentional misalignments generally do not significantly distort the beam profile and coherence in diffraction applications [61], it is not a priori clear what the possible influences to the pulse duration could be.

This letter has two parts. First we present a numerical investigation of the temporal distortions arising from tilted and/or displaced magnetic solenoid lenses, and discuss the findings. Second, we explain an experimental alignment procedure allowing to precisely arrange a solenoid lens in a collinear and centered way with respect to a given electron beam. For the example of a single-electron time-resolved diffraction beamline [33], we estimate that this procedure minimizes the alignment-induced temporal aberrations to a level below one femtosecond. This is a general prerequisite for eventually advancing 4D electron imaging, be it with microscopy or diffraction, to the few-femtosecond domain of primary structural dynamics in molecules and condensed matter or eventually to the attosecond domain of electronic motion [69].

We start with the simulations. The electron source is modeled in resemblance of the latest tight-focusing version in our laboratory, optimized for ultrashort and coherent single-electron emission without space charge [21, 33]. The initial conditions of the simulation's virtual source are single-electron pulses with a beam radius of 3.5 μm (rms) and a transverse velocity spread of 140 km/s (rms) at a central energy of 70 keV, i.e. with a divergence of about 1 $mrad$ (rms). The emission duration, determined by the duration of the femtosecond laser pulses applied for photoemission, and the longitudinal velocity spread are artificially set to zero, so that the pulse duration in free propagation would be infinitely short all the time; this setting is made in order to study the lens distortions exclusively without superimposing the dispersive broadening caused by the longitudinal emission statistics [21], like we did it before [60]. The magnetic lens is approximated with one single coil having a diameter of 60 mm and a distance from the virtual source of 17 cm. The electrical current and hence the focal distance are chosen such that an "isochronic" condition, i.e. coincidence of the spatial and temporal focus, occurs at a distance of 31 cm after the coil. This corresponds to a magnification of 1.8 : 1, which is close to the magnification of about two predicted analytically [60].

Figure 3.11 shows the results. The upper panel in figure 3.11(a) depicts the evolution of the beam diameter during propagation and shows a focus at $z \approx 48$ cm after the source. The resulting spatial focus size does not change noticeably with misalignment of about 1° and 1 mm. In contrast, the lower panel in figure 3.11(b) shows the evolution of the pulse duration for the perfectly oriented lens (blue), for a tilt of 0.05° (violet) and for 0.1° (red). Already such small angles start making the temporal focus disappear. A more systematic evaluation is shown in figure 3.12.

For different tilt angles between 0° and 2°, the pulse duration at the spatial focus is plotted on a color scale while varying the two displacements along the x and y axis. A tilt of 1° or a displacement of 1 mm (2% of the lens diameter) is already sufficient to broaden the electron pulses by about 50 fs (full width at half maximum). Interestingly, there are conditions in which the angular misalignment and the lateral displacement can partially compensate each other. However, these minima are a little larger than the minimum without any tilt and also difficult to find experimentally. The lowest distortions and tidiest conditions are achieved if the lens is simultaneously aligned perpendicular and central to the electron beam.

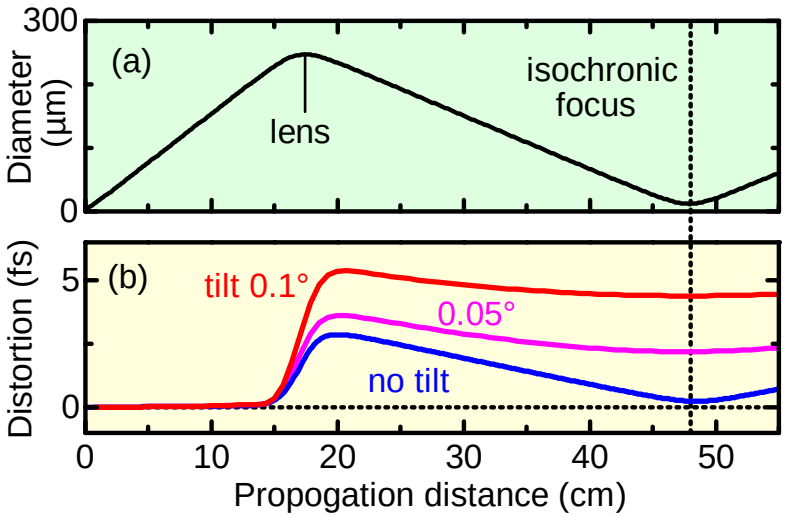

Figure 3.11: Interplay of spatial and temporal focusing in a solenoid lens. (a) The electron beam from the femtosecond source is divergent and a magnetic lens is used for refocusing onto a diffraction sample (dotted). The beam diameter (full width at half maximum) first increases and subsequently decreases. (b) The evolution of the temporal distortions (full width at half maximum) depends on the misalignment in the lens. For perfect alignment (blue), there is a temporal focus at the same location as the spatial focus. If the lens is tilted (violet and red), the pulses become longer due to temporal distortions.

Hence we here, in the second part of this letter, describe an experimental procedure for aligning a solenoid lens around a given electron beam. The concept is based on a reversal in current in combination with lateral displacement scans; this idea was inspired by an earlier report in 1964 using rotation reversal [70]. Basically, if the B-field of a perfectly aligned magnetic lens is reversed, symmetry requires that

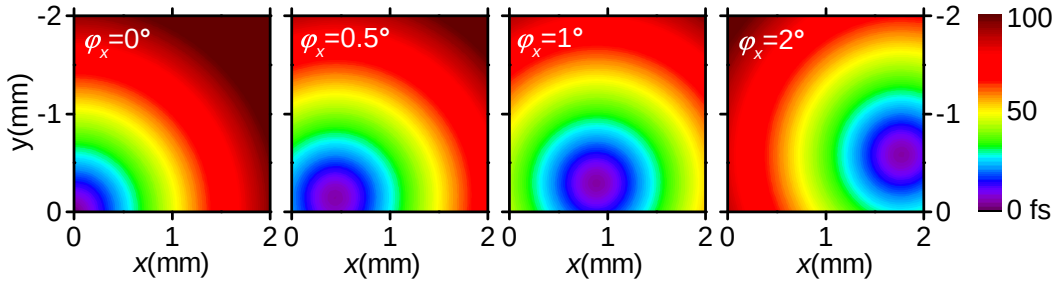

Figure 3.12: Temporal distortions (full width at half maximum) of a magnetic solenoid lens caused by combinations of tilt and displacement. For further details see the text.

there is no change in beam displacement on a distant screen. This, however, changes with misalignment, offering the necessary feedback for an alignment technique.

The experiment consists of a single-electron source based on photoelectric emission and electrostatic acceleration to 70 keV in a vacuum chamber at a pressure of about 10^{-9} $mbar$. For simplicity, we use the ultraviolet light from a deuterium lamp for electron generation instead of the femtosecond laser. This generates an electron beam of somewhat lower emittance, but the beam quality is still sufficient for the alignment procedure. The solenoid (AccTec BV) consists of 353 windings and is placed around a vacuum tube with the beam inside. The inner diameter is 85 mm and the length is 60 mm; water-cooling is applied for heat removal. The in-and-outgoing wires are guided closely and in parallel to each other, in order to cancel their fields. The solenoid can be displaced along x and y using mechanical translation stages. Tilts around the x and y axis are achieved by letting the whole assembly stand on the optical table with three posts of adjustable height. We note that instead of mechanically moving the solenoid, we could have also used a set of bending magnets for aligning the beam with respect to a mechanically fixed lens. This was avoided for simplicity, but might be a more practical approach for rigidly constructed electron microscopes or for particle accelerators with heavy lens assemblies.

The constant current for the solenoid's magnetic field is provided by a stabilized power supply (PSM-2010, GWInstek). The periodic field reversal is achieved by an electronic switching circuit based on metal-oxide-semiconductor field-effect transistors (IRF9540 and BUZ11), which are well capable of handling the typical power

in our lenses ($20 - 100\ W$). The current is reversed at a repetition rate of about $5\ Hz$. A varistor circuit is applied to get rid of the magnetic field energy (up to $1\ J$) at each current reversal. At a distance of $127\ cm$ after the lens, the electron beam is recorded with a phosphor screen and a high-resolution camera (TemCam-F416, TVIPS GmbH) at a readout rate of $1\ Hz$. We hence observe two spots on each image, one for each sign of the field. The alignment procedure consists of these five steps:

1. We switch off the current in the lens and note the position of the unfocused electron beam on the screen. We call this the center position.

2. We set the lens to the desired focus strength and activate the reversal circuit; two spots appear. We shift the lens along x in several steps; the two spots move along two approximately linear trajectories (see figure 3.13(a)).

3. By using the two displacements along x and y in combination, we can make the two spots coincide. Movement forth and back along x now produces the cross-like pattern with an overlap region shown in figure 3.13(b).

4. Typically, this overlap position of the two beams is not at the center position noted in step 1. We increase φ_x by some small amount and repeat steps 2-3. The new crossing point is now either closer or farther from the center position. If closer, we continue with increasing φ_x, if more distant we reduce it. By using φ_x and φ_y and each time repeating steps 2-3 we can direct the crossing point to the center position.

5. Movement forth and back along x now produces the cross pattern shown in figure 3.13(c), having the crossing point at the center position. The lens is now aligned.

With some skill, it takes about 15 *min* to achieve convergence, depending on the desired accuracy of determining the beam centers. Effectively, the procedure leads to a unique condition in which the electron beam travels in the center and perpendicularly to the magnetic field's rotational symmetry. At these conditions, as shown above, the temporal distortions are minimal.

In order to estimate the accuracy that we can expect, we invoke the simulations again. We find that the beam position on the screen, i.e. the measured

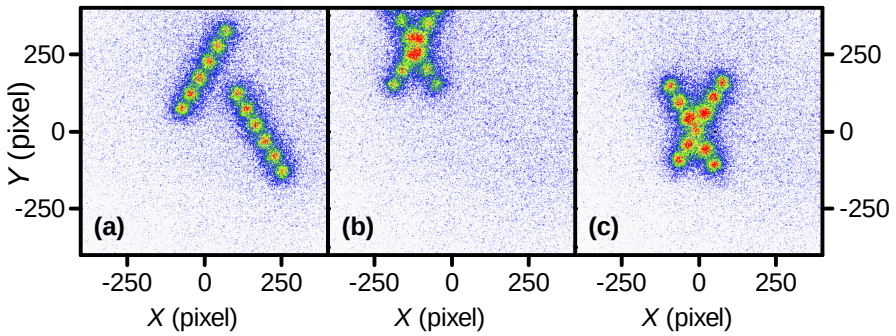

Figure 3.13: Experimental results of the here demonstrated procedure for lens alignment. The magnetic field is periodically reversed and two separate spots are observed on a screen if the integration time is long enough. Each displayed picture is an overlay of six exposures differing by small displacements of the lens. (a) The magnetic lens is totally misaligned. (b) Intermediate stage during alignment. (c) The lens is aligned and the two spots overlap centrally on the beam axis. Temporal distortions are minimized to a sub-femtosecond level.

spot's distance from the optical axis, scales approximately linear with the amount of misalignment. The slope between the screen position and the tilt angle is about 21 mm/deg. The slope between the screen position and the lens displacement is about 11 mm/mm. The accuracy with which we can determine the beam's center on the screen is about two or three pixels, i.e. about 40 μm. We hence obtain an expected accuracy of about 0.002° for the tilt and about 4 μm for the lens displacement. This, of course, requires good enough mechanics to realize in practice.

At the sample (31 cm after the lens), the temporal aberrations are found to also scale about linearly with the tilt angle and with the lens displacement, respectively. The slope between the temporal distortions and the tilt angle is about 44 fs/deg. The slope between the distortions and the lens displacement is about 47 fs/mm. For the above estimated accuracy of lens adjustment, the associated temporal distortions are therefore 0.1 fs and 0.2 fs, respectively. This result shows that a proper lens design and alignment allows for steering and imaging the few-femtosecond and eventually attosecond electron pulses that may be generated sometimes [43].

It seems that our alignment technique could generally work with any magnetostatic fields of rotational symmetry, for example magnets with pole pieces in an electron microscope, provided that field reversal leads to different trajectories that

are discernible on a screen. We also predict that our procedure will be useful for aligning the microwave cavities recently used to compress ultrashort electron pulses in time [26, 28, 71–73]. In these time-dependent elements, the transient magnetic fields have a rotational component caused by the longitudinal displacement current. Although the (de-) focusing mechanism is different from the magneto-static case [74], a change of sign (by a 180° change of phase) will nevertheless lead to a change in beam propagation in case of misalignment, offering the opportunity to use the here described procedure for optimization. However, a precise laser-microwave synchronization is required [75, 76].

We conclude with an outlook. In optics, the production of extremely short laser pulses was only possible by extensively characterizing and compensating numerous types of spatio-temporal and chromatic distortions, including higher-order chirp and chirp-transfer in nonlinear interactions [77], pulse front tilt [78] and carrier-envelope phase [79], among others. The combined optimization of everything has been essential for reaching the few-femtosecond and attosecond regimes of optics. The same effort is probably required for letting electron pulses catch up, for advancing four-dimensional electron microscopy and diffraction into the regime of few-femtosecond dynamic and below. The here reported findings on the temporal distortions of charged-particle lenses and the experimental procedure for alignment should help coming along towards that goal.

3.5 Femtosecond single-electron pulses generated by two-photon photoemission close to the work function

This chapter is also submitted to New Journal of Physics [80] and currently in review.

I want to thank Lamia Kasmi, who was a master student in our laboratory at this time and helped including and aligning the nonlinear optical parametric amplifier (NOPA) in our apparatus [81].

Abstract: Diffraction and microscopy with ultrashort electron pulses can reveal atomic-scale motion during matter transformations. However, the spatiotemporal resolution is significantly limited by the achievable quality of the electron source. Here we report on the emission of femtosecond single/few-electron pulses from a flat metal surface via two-photon photoemission at $50 - 100\ kHz$. As pump we use wavelength-tunable visible 40 fs pulses from a noncollinear optical parametric amplifier pumped by a picosecond thin-disk laser. We demonstrate the beneficial influence of photon energies close to the photocathode's work function for the coherence and duration of the electron pulses. The source's stability approaches the shot noise limit after removing second-order correlation with the driving laser power. Two-photon photoemission offers genuine advantages in minimizing emission duration and effective source size directly at the location of photoemission. It produces an unprecedented combination of coherent, ultrashort and ultrastable single/few-electron wave packets for time-resolving structural dynamics.

Introduction: The direct visualization of atomic motion in space and time in pump-probe diffraction requires a probing wavelength shorter than atomic distances; in addition, the pulse duration should be shorter than the fastest dynamics of interest, i.e. tens to hundreds of femtoseconds. Pump-probe electron microscopy and diffraction [43, 58, 59, 82] offer these capabilities, evident in a large range of recent discoveries, for example in the fields of condensed-matter physics [27, 83–85], chemistry [86–89] or surface science [90, 91]. On the one hand, time-resolved electron diffraction with brightest/densest electron packets [92] aims for single-shot imaging of macromolecular dynamics at hundreds-of-femtosecond resolution [8]; this requires compensation of space charge broadening with microwave-based compression or streaking techniques [71, 93, 94]. The finally achievable pulse duration and degree of coherence are limited by the irreversible parts of these Coulomb interactions. On the other hand, single-electron pulses [21, 22] avoid space charge effects entirely and, when combined with dispersion control [26], potentially offer few-femtosecond resolution and below, according to simulations [6, 28–30]. This may come at the cost of sample restrictions [8], but pump-probe diffraction with single electrons was recently achieved on graphite, suggesting this concept's feasibility at least in the regime of reversible condensed-matter dynamics [23].

In the absence of space charge, the decisive matter becomes the shape and size of the initial phase space after electron generation by femtosecond photoemission. All subsequent beam manipulations, for example with magnetic lenses or temporal compression, cannot practically reduce the initial phase space volume. The physics of photoemission hence determines the best achievable compromises at target, for example between pulse duration and monochromaticity [76], between coherence and beam size [61] and between divergence and temporal distortions [60], among others [33]. A fundamental study and optimization of photoemission in the femtosecond regime is therefore essential for advancing ultrafast imaging with electrons towards novel resolution regimes.

Here we investigate the use of two-photon photoemission instead of the commonly applied one-photon process for the ultrafast emission of diffraction-capable single-electron and few-electron pulses, generated at high repetition rate. We show that electron dispersion, incoherence and temporal distortions are all minimized simultaneously at photon energies approaching half of the photoemitter's work function. In addition, experimental optimization of emittance and emission duration becomes extremely simple in the two-photon regime, as a consequence of the nonlinear coupling between the optical pulses' peak intensity and the resulting current of femtosecond electrons.

Femtosecond photoemission: Ultrashort single-electron pulses are usually produced from flat metal photocathodes via photoelectric emission driven by femtosecond optical pulses at an ultraviolet wavelength[33]. While this scheme is practical and very stable [23], the energy spread of photoelectrons is typically much larger (hundreds of meV) than that of the driving laser pulses (tens of meV) [26, 68]. This causes dispersive broadening of single-electron wave packets during acceleration and propagation [68]. After a wave packet compressor [26, 28, 29], the achievable pulse duration is directly affected by the time-bandwidth product before the compressor [33]; a minimized longitudinal emittance is therefore essential for ultimate pulse durations in the few-femtosecond and maybe attosecond regimes [43]. Also, the initial electron beam typically shows significantly more transverse momentum than the generating laser pulses. This causes the electron beam to diverge and reduces the ratio of transverse coherence to beam diameter at the diffraction target, limiting the ability to resolve the larger unit cells of complex materials [61].

A main reason for these two types of phase space broadening during photoemission is mismatch between the laser's photon energy and the cathode material's work function [21] in combination with imperfections of the emitter material. In a simplified picture, the laser photons are absorbed in the metal and produce charge carriers that travel towards the surface. This, however, involves dephasing and scattering from impurities [95, 96], homogenizing the electron energy spectrum and directions over all available phase space. Ejection into free space occurs for such carriers, or parts of their wave function, that have enough energy exceeding the material's work function. In the single-electron regime, the emitted wave packet hence covers all the energetically available phase space continuously [21]; simply speaking, the laser's temporal and spatial coherence are lost in the photoemission process. The lower the difference between work function and photon energy, the lower is the increase of emittance when converting photons to electrons using photoemission from realistic metal surfaces.

In summary, there are three conditions for optimizing a photoemission-based femtosecond single-electron source. First, the photon energy should be close to the work function for avoiding excess bandwidth [21]. Second, the photoemission time, i.e. laser pulse width, should be optimized as a compromise between shortest duration and smallest bandwidth, using Fourier-limited optical pulses [21, 26]. Third, the area and angular spread of the photoemission process should be minimized for maximizing transverse coherence [61].

Two-photon photoemission: These three conditions are difficult to realize in an experiment. First, production of ultrashort and wavelength-tunable laser pulses is challenging in the ultraviolet [97–99], especially for high repetition rates in the hundreds-of-kHz regime. Second, minimizing the duration of photoemission requires chirp compensation at the location of the photocathode, i.e. in a vacuum environment, where optical pulse metrology is difficult. Characterizing the electron pulses themselves using laser-based streaking [61] or ponderomotive scattering [100, 101] is not routinely applicable in many laboratories. Third, minimizing the emission area to μm-sized diameters [23] is also difficult, because time-consuming waist scans with a well-aligned magnetic lens system [56] are required for a precise determination [61].

These practical difficulties with conventional photoemission sources motivated the present research and application of a two-photon process for electron emission. Such

an approach was briefly mentioned earlier [23, 59, 102, 103], but neither details were given nor were tunable pulses applied. The expected advantage of two-photon photoemission is a second-order scaling between electron generation efficiency and the optical peak intensity at the photocathode material. The shorter the duration and the smaller the focus, the larger an electron current is measured. This simple relation should allow finding the optimum emission conditions easily in the experiment, without resorting to temporal electron pulse characterization or waists scans.

These questions remain: What optical intensity and pulse energy is required? How to generate the optical pulses at tunable photon energies? Are there thermal contributions to the electron current? How stable is the current over the many hours required for a pump-probe single-electron diffraction study [23]? Is the transverse coherence comparable to conventionally generated beams [61]? What is the relation between photon excess energy and beam emittance? And finally, is two-photon photoemission a practical approach for pump-probe single-electron diffraction of reversible condensed-matter dynamics? The present letter aims at answering these questions.

Experimental setup - tunable visible NOPA pulses and electron beam metrology: The experimental setup consists of a picosecond laser source, a frequency conversion unit, an electron source and a diffraction beamline with single-electron area detector. The picosecond laser is a regenerative Yb:YAG thin-disk amplifier producing 330-μJ pulses at a central wavelength of 1030 nm [36], delivering 0.8 ps pulses at optimized conditions [36] and 1.0 ps in the present experiments. The laser's repetition rate is tunable between $50-400$ kHz and was set to 100 kHz, appropriate for pump-probe single-electron diffraction [23]. The photocathode is a 20-nm gold layer on a sapphire substrate. Gold's work function at such conditions is about 4.3 eV [21], corresponding to an optical wavelength of 290 nm. Hence, for two-photon photoemission, we need optical pulses that are tunable in the visible spectral range around and below 580 nm. For generating these pulses, we apply a noncollinear optical parametric amplifier (NOPA) based on an earlier design [104], but specifically optimized for pumping with the picosecond pulses. A white-light continuum is difficult to achieve with long pump pulses [105], but is here successfully established using a 4-mm YAG crystal pumped with pulse energies of about 7 μJ, focused using an $f = 80$ mm lens. Similar to earlier results [106], the con-

tinuum smoothly covers the range $480 - 950\ nm$ and makes an ideal seed light for the NOPA process in a 2-mm thick type-I BBO crystal at 37°. The pump pulses at 344 nm are derived from the thin-disk laser by frequency-tripling in a sequence of two group-velocity-compensating BBO crystals [104], a 0.8-mm thick type-I crystal at 23.5° for second harmonic generation followed by a 1.5-mm thick type-II crystal at 62.8° for sum-frequency mixing. Pulses are compressed using a double-pass through two fused-silica prisms with a 68.7° apex angle at a separation of $\sim 65\ cm$. A dispersion-free autocorrelator [107] is applied for pulse characterization.

In this ps-driven NOPA, the ultraviolet pump pulses at 344 nm have a duration only slightly shorter than the fundamental pulses from the thin-disk laser, about $0.6 - 1\ ps$. Therefore, amplification of the chirped white-light is extremely broadband; spectra with Fourier limits down to 5.3 fs could be directly generated with a pulse energy of up to 1 μJ. This represents a factor of 150 in potential shortening of the ps-pulses from the high-power Yb:YAG disk laser. The particular spectrum used for photoemission experiments is shown in Fig. 3.14(a) and has a Fourier limit of 7 fs. In order to produce longer and tunable pulses for electron emission, some narrower parts of this spectrum are selected in the Fourier domain. To this end, the NOPA beam is focused through the two compressor prisms onto the end mirror, where an adjustable slit is located for filtering the spectrum; see Fig. 3.14(c). This selects wavelength-tunable pulses of adjustable bandwidth with energies of several nJ. Figure 3.14(b) shows the series of spectra applied for photoemission, continuously covering the spectral range of $505 - 580\ nm$ at photon energies of $2.1 - 2.5\ eV$. The slit width is chosen to select a spectral width corresponding to a Fourier limit of $\sim 40\ fs$. The effective duration of the cathode's two-photon emission process is $\sqrt{2}$ times shorter, about 30 fs. This is close to the optimum for generating shortest electron pulses assuming high-field electrostatic acceleration ($10 kV/mm$) [21]. Slight adjustment of the prism compressor for each selected wavelength is sufficient to compensate the NOPA output's higher-order dispersion.

For electron generation, the optical beam is expanded to a full-width-at-half-maximum diameter of $\sim 8\ mm$ and sent into the electron source's vacuum chamber through a 3-mm thick fused-silica window. A $f = 35\ mm$ lens within the vacuum environment focuses the beam onto the photocathode, a 20-nm gold layer on the far side of a 1-mm thick sapphire substrate. The electrons are accelerated to 70 keV with an electrostatic field of $\sim 2.8\ kV/mm$. The electron beam passes through an

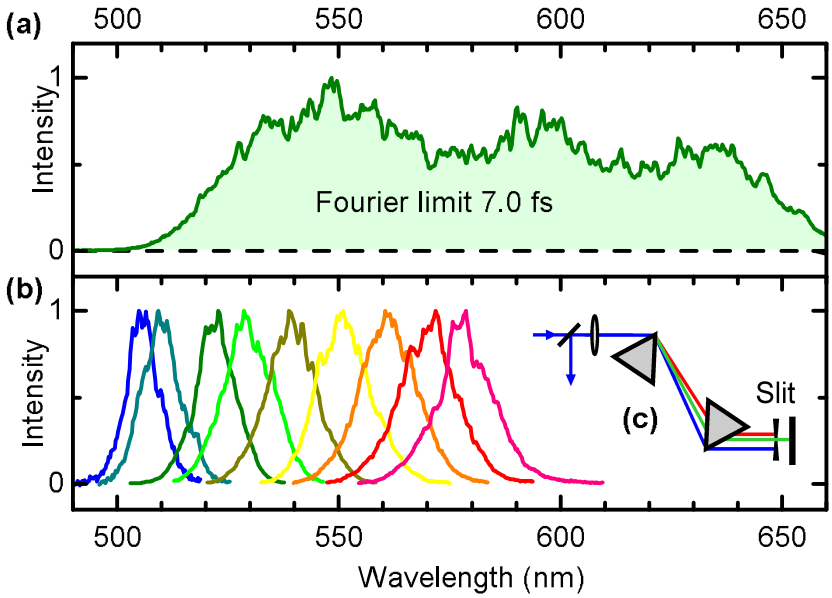

Figure 3.14: Performance of our NOPA system driven by picosecond pulses from an Yb:YAG disk laser. (a) Broadband output spectrum. (b) Tunable spectra with Fourier limits of $\sim$ 40 fs for tunable photoemission studies. (c) Slit arrangement for spectral filtering in the Fourier domain.

anode hole with a diameter of 8 mm. At a distance of 1.42 m, a phosphor screen and camera are used to record the electron beam for each optical central wavelength.

Results - Quadratic emission increase and two-photon cross section: We first show results on two-photon photoemission using sub-ps pulses at 515 nm produced directly via second-harmonic-generation at 50 kHz, and report on our findings with the tunable NOPA pulses at 100 kHz later. Figure 3.15(a) shows the number of emitted electrons per optical pulse in dependence on the applied peak intensity. The latter is estimated from the optical pulse duration, incident power, repetition rate, focus size and Fresnel losses of the lens and cathode substrate within the vacuum chamber. As expected, there is a quadratic dependence of the electron yield with pulse intensity. Less than 1 nJ of incident optical pulse energy is well sufficient for emitting more than one electron per pulse. Thermal effects at the photocathode are therefore negligible; this is also evident from the quadratic dependence in Fig. 3.15(a). The effective radius of the electron-emitting area is determined by

knife-edge scans of the magnetically focused electron beam and by waist scans [61]; we obtain a full-width-at-half-maximum of $\sim 8.5\ \mu m$ or $\sim 3.6\ \mu m$ rms, the common definition in ultrafast electron optics [62]. This measurement is resolution-limited and the reported value is therefore an upper limit.

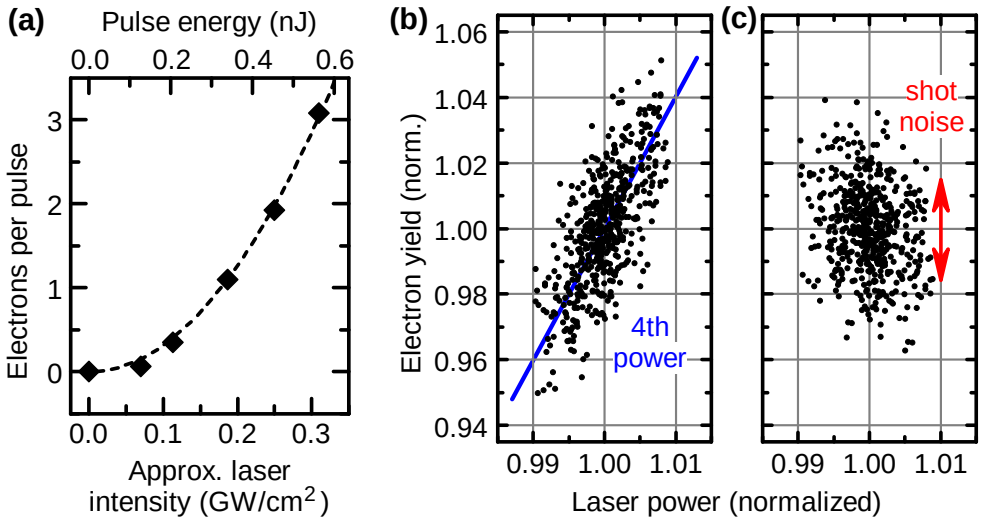

Figure 3.15: Two-photon photoemission at 515 nm and its stability. (a) Number of electrons per pulse obtained with varying laser pulse energy and estimated peak intensity incident on the gold layer. The clear quadratic dependence (dashed) demonstrates that two-photon photoemission is the predominant process. (b) Correlation between electron yield and fundamental laser power. The fourth-order correlation is expected from the sequence of two second-order processes, second-harmonic generation in BBO followed by two-photon photoemission at the gold layer. (c) The residual noise is uncorrelated, 1.3% rms, and limited by shot noise.

Results - stability: After about one hour of conditioning, the long-term degradation of the source is less than 1% per hour. On shorter time scales, some fluctuations originate from the thin-disk laser's output noise. Figure 3.15(b) shows the correlation between the optical power at 1030 nm and the electron yield taken every ten seconds over a two-hour period. The correlation coefficient is ~ 4, as expected from the effectively fourth-order nonlinear conversion process (unsaturated second-harmonic generation followed by two-photon photoemission). Interestingly, when removing this correlation numerically by dividing the electron yield by the fourth

power of the measured optical power, there remains a residual, laser-independent noise of the electron source of 1.3% rms (see Fig. 3.15c). This is a consequence of shot noise. An average of 0.13 $electrons$ were generated per pulse at a 50 kHz repetition rate and images were integrated for one second; hence there are 6500 electrons per image. Assuming that the electron emission follows Poisson statistics, the shot noise is about $\sqrt{6500}/6500 \approx 1.2\%$. This is very close to the measured value. We conclude that our two-photon-driven electron source operates close to the quantum-limited regime of stability when numerically compensating for the measurable slow drifts of the laser power.

Results - Emittance and pulse duration: We next report the results with tunable NOPA pulses, aiming for a decrease of emittance when approaching half of the work function. To this end we measured the direct, unfocused electron beam radius as a function of the photoemission pump wavelength. Using the tunable pulses of Fig. 3.14(b), we obtain the beam results shown in Fig. 3.16(b), left scale. Immediately evident is a clear shrinkage of the beam size with decreasing photon energy, demonstrating a reduction of emittance when less excess energy is available. The second finding is kind of a threshold when approaching the work function; no beam smaller than ~ 1.8 mm radius could be generated with our system.

Before we discuss these results, we deduce from the measured beam radius y'' on the screen the photocathode's transverse momentum spread and emittance. We consider a non-relativistic approximation and the geometry depicted in Fig. 3.16(a). The optical focus size (a few μm) is negligible compared to the beam radius at the screen, millimeters. An electron emitted with a transverse velocity component $v_\perp$ moves along a parabolic trajectory in the cathode-anode region (L_{acc}) and later along a linear trajectory in the drift region (L_{drift}). The anode hole has a defocusing effect on the electron beam that can be approximated with a focal length of $f \approx -4 \cdot L_{acc}$ [68]. In our experiment, $L_{acc} \approx 25\ mm$, $E_{acc} \approx 2.8\ kV/mm$ and $L_{drift} \approx 1.42\ m$. The forward velocity after acceleration is $v_0 \approx 0.47\ c$.

Let us calculate the relation between initial transverse velocity $v_\perp$ and the point of incidence y'' at the screen in a non-relativistic approximation. In the cathode-anode region, the acceleration is eE_{acc}/m_e. The time t_{acc} that an electron spends in the anode-cathode region is $t_{acc} \approx \sqrt{2m_e L_{acc}^2/(eE_{acc})}$, about 300 ps in our experiment. The small variations of t_{acc} that are caused by the initial distribution of forward

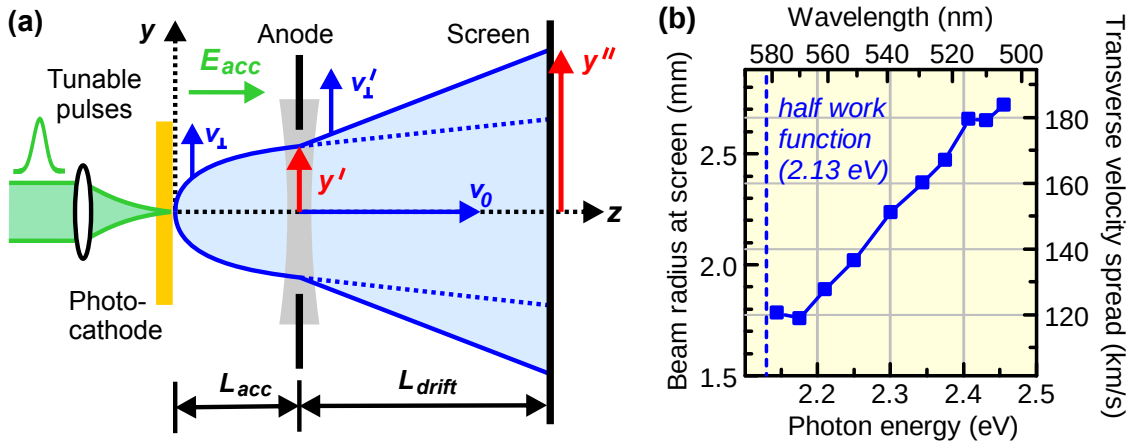

Figure 3.16: Experimental geometry and results on wavelength-dependent electron beam divergence. (a) Tunable femtosecond pulses from the NOPA (green) impinge on a gold photocathode (yellow). Electrons are generated by two-photon photoemission and accelerated in an electrostatic field E_{acc}. After an anode producing a defocusing lens (grey), the beam expands towards a screen. (b) Measured electron beam size and corresponding initial transverse velocity spread in dependence on the excitation wavelength and photon energy. A clear decrease towards half of the work function (dashed) indicates the superior electron beam quality obtainable with tunable NOPA pulses and two-photon photoemission.

velocities amount to less than one picosecond and are therefore neglected. After t_{acc}, the position y' of the electron at the anode plane is $y' \approx v_\perp t_{acc}$. The anode hole's defocusing effect ($f \approx -4L_{acc}$) and the further beam propagation over a distance L_{drift} can be described by ray transfer matrices. At the screen, the final position y'' and the transverse velocity $v''_\perp$ are given by

$$\begin{pmatrix} y'' \\ \frac{v''_\perp}{v_0} \end{pmatrix} = \underbrace{\begin{pmatrix} 1 & L_{drift} \\ 0 & 1 \end{pmatrix}}_{free\ drift} \underbrace{\begin{pmatrix} 1 & 0 \\ \frac{1}{4L_{acc}} & 1 \end{pmatrix}}_{anode\ hole} \underbrace{\begin{pmatrix} y' \\ \frac{v_\perp}{v_0} \end{pmatrix}}_{before\ anode} . \tag{3.5}$$

Inserting the basic quantities of the experimental geometry, we obtain

$$y'' = [\sqrt{\frac{2m_e L_{acc}^2}{eE_{acc}}}(1 + \frac{L_{drift}}{4L_{acc}}) + \frac{L_{drift}}{v_0}]v_\perp. \tag{3.6}$$

This describes a linear relation between an electron's incidence point on the screen (y'') and its original transverse velocity after photoemission ($v_\perp$). Therefore, in terms of distributions, the measured radial beam profile at the screen reveals the distribution of transverse velocities at the photocathode. A measured radius of the beam is hence directly converted to the spread of transverse velocity at the electron emitter. The results are shown in Fig. 3.16(b) with the right-hand scale.

These results, including trend and order-of-magnitude, compare very favourably to the one-photon data of Aidelsburger and co-workers [21]. For a photon energy close to the work function, or here half of the work function, emittance is reduced: shorter, more coherent and less spatiotemporally distorted electron pulses are produced. Assuming that the longitudinal velocity spread is similar to the transverse one [21], i.e. a half-spherical initial shape of the initial phase space, sub-100-fs pulses are achievable with 10 kV/mm electrostatic acceleration [21] without requiring microwave compression [26] and advanced synchronization [76]. More importantly, if single-electron pulse compression is applied with time-dependent microwave fields [26], any smaller phase space volume in the time/energy domain before compression either implies an improved monochromaticity or shorter pulses at target [26].

Transverse emittance determines the ability of electron diffraction to resolve atomic motion within complex unit cells, because only such atoms can mutually interfere that are not separated by significantly more than one coherence length. Nano-scale needle emitters are ideal in that aspect, but suffer from spatiotemporal correlations in the beam profile [65, 66] making pulse compression difficult. It is possible to apply apertures to dense electron pulses for improving coherence, but this implies space charge effects before the aperture that in part irreversibly reduce the ability for temporal compression. Our two-photon source's transverse normalized emittance is $\epsilon_\perp = c^{-1}\sigma_\perp v_\perp$ with $\sigma_\perp$ and $v_\perp$ as rms values [62]. Assuming that the NOPA pulses at the optimum wavelength of 570 nm are focusable down to a full width of 5 μm ($\sim$ 4 μm $1/e^2$-radius or $\sim$ 2.1 μm rms) at the gold layer, similar to what is achievable with 400-nm pulses [23], we expect an effective source size of $\sim$ 1.5 μm rms and an emittance of $\epsilon_\perp \approx 0.6$ nm. This is as good as our recently reported one-photon-driven ultrafast single-electron source [23] with coherences exceeding biomolecular dimensions [61], but here without any difficulties in reaching these values experimentally, namely without repetitive waist scans or electron pulse metrology. There are no significant spatiotemporal distortions or space-charge-induced

emittance increases, hence we expect compressibility of the electron pulses to the few-femtosecond, potentially attosecond regime of duration [26, 33].

Intriguing to us is the apparent threshold of transverse velocity spread when approaching half of the work function. The measured 120 km/s rms corresponds to an energy bandwidth of 0.04 eV. This residual spread and threshold might potentially originate from an inhomogeneous distribution of effective work functions, contributions by gold's Fermi velocity, surface roughnesses, inhomogeneous distributions of initial acceleration trajectories, or from the femtosecond emission duration via the uncertainty relation. Further theoretical considerations are required here [108]. The optical pulse energy of ~ 0.3 nJ required for emitting one electron per pulse (see Fig. 3.15a) corresponds to $\sim 8 \times 10^8$ photons. About half of these are absorbed in gold and produce in the excited volume a density of hot charge carriers of $\sim \ 10^{21}$ cm^{-3}; this is significant as compared to the metal's basic charge density. Nevertheless, our results show that the corresponding screening and scattering processes during femtosecond photoemission are insignificant for the emittance and energy distribution of two-photon emitted single electrons.

Conclusion: In conclusion, an optimized noncollinear parametric amplifier produces energetic pulses with a 7 fs Fourier limit even with ps-long pump pulses. More narrowband tunable pulses are generated by limiting the spectrum in the Fourier plane of the prism compressor. For generating femtosecond electron pulses, two-photon photoemission is found superior to the one-photon emission process used so far in our laboratory [43]. The practical advantages are an easy optimization of optical pulse duration and focus diameter directly at the site of electron generation within the vacuum system. Temporal electron pulse metrology and waists scans can be avoided. In addition, the experiment becomes significantly simpler. First, one optical frequency conversion stage is replaced by a bandwidth-free process in situ at the photocathode. Second, the optical pulses can be longer, since the duration of electron emission is intrinsically reduced by about $\sqrt{2}$. Third, the effective emission area is by a factor of two smaller than the optical focus, alleviating the need for high-quality UV optics within the vacuum system. Fourth, the direct correlation of electron yield to laser power drifts without thermal contributions or saturation effects can effectively provide a short-term and long-term stability approaching the shot noise limit, without particular efforts for laser stabilization.

The general results, namely that the transverse momentum spread with two-photon photoemission is similar to that of single-photon emission at twice the photon energy, and that emittance decreases towards half of the work function with an evident threshold, should contribute to better understanding photoemission in general, for the benefit of a wide range of applications including particle acceleration, electron microscopy or quantum optics with electrons.

3.6 Sample chamber

For electron-diffraction experiments, it is essential that the samples can be properly positioned with respect to the incident electron beam in order to fulfill the Bragg-condition. The heart of the sample chamber is a non-magnetic six-axis sample positioning system (SmarPod) that was developed together with the company SmarAct GmbH. The SmarPod is constructed similar to a hexapod and allows motion in all six degrees of freedom (three translational x, y, z and three rotational $\theta_x, \theta_y, \theta_z$). The travel range for x, y is 42 mm, for the vertical dimension z it is 24 mm, for the tilt θ_x, θ_y it is 20° and for the rotation θ_z it is 360°; to obtain the rotation around the full axis of z, the hexapod is combined with an additional rotary table (SR-5714-S-UHVT-NM). All axes are controlled by piezoelectric motors and the resolution of the system equals about 1 nm. We know from our first-generation apparatus UED1 [25] that it is crucial to have no magnetic parts near the electron beamline, and especially no moving magnetic parts. Therefore all components used in the SmarPod are made of non-magnetic materials and the movement is provided by piezoelectric motors.

The sample chamber has a diameter of 406 mm and the floor consists of a M6 thread pattern similar to optical tables to easily attach, e.g., mirrors or diagnostics. Fig. 3.17 shows a top-view of the chamber with the lid removed. The chamber has several ports to connect various equipment and appropriate windows to excite the specimen.

The top lid has two viewports, in order to provide visible access to the sample and the possibility to excite the sample with tilted pulses for grazing-incidence diffraction geometry (see chapter 3.7). To one viewport, a CMOS-camera (digital

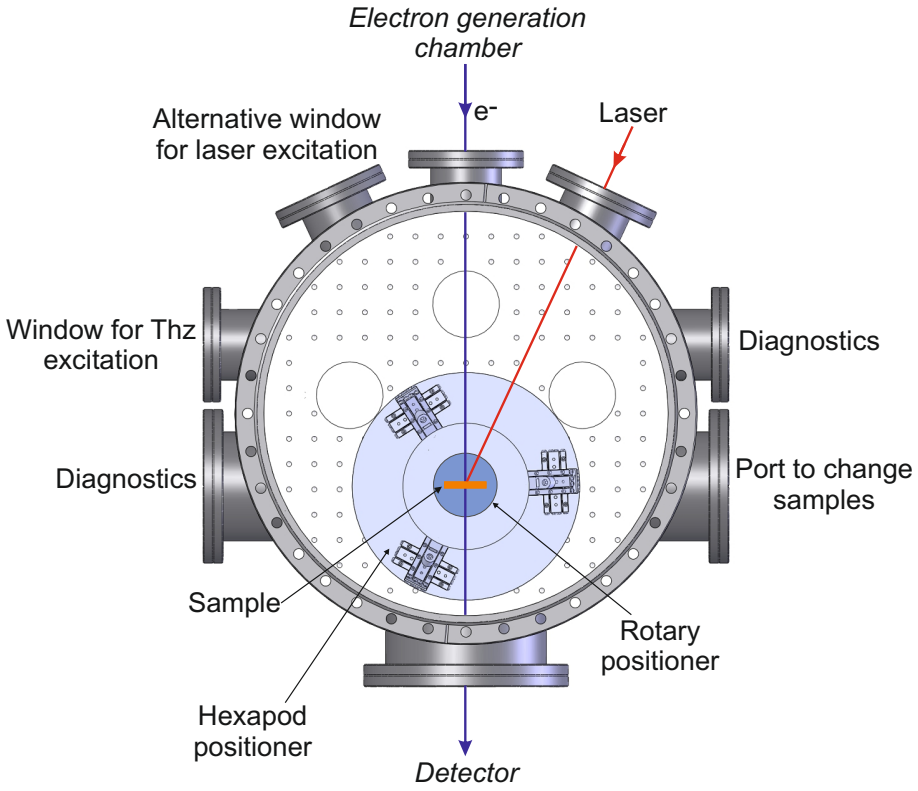

Figure 3.17: Top view of the sample chamber with the lid removed. Furthermore the beam paths for sample excitation in electron transmission geometry (cf. chapter 3.7) are illustrated.

high resolution camera DHHV3151UC-ML, Daheng) combined with a macro lens (Tamron AF 180mm Nikon F/3.5 SP Di LD IF 1:1 Macro) for 1:1 imaging of the sample is attached. The sensor has a size of 6.4 $mm \times 4.8$ mm and a resolution of 2048×1536 $pixels$ with a corresponding pixel size of 3.2 $\mu m \times 3.2$ μm [109]. This allows a high-resolution close-up view of the sample, which is very useful for, e.g., finding the spatial overlap between the laser and the electron beam (see chapter 4.5).

3.7 Concepts for sample excitation

In a time-resolved electron diffraction experiment, you have two possibilities to place the sample to the electron beam, i.e. in transmission or grazing-incidence geometry, as shown in figure 3.18. In transmission geometry (3.18(a)), you have to use very thin samples to assure that enough electrons pass through them to produce a

diffraction image. The penetration depth of electrons depends on their energy, hence a high acceleration voltage is useful (cf. chapter 1). For energies of 100 keV the sample thickness can be of the order of 100 nm, making sample preparation less time consuming and challenging than for lower electron energies. In grazing-incidence geometry, the electron beam impinges on the sample at very small incident angles (see fig. 3.18(b)), typically $1-5°$. Bulk samples can be studied in this way. This method, however, is very sensitive to the sample surface quality and you have to take care of appropriate surface treatment (like sputtering or annealing). Another drawback in grazing-incidence geometry is that you loose the lower half of the diffraction image, because it is blocked by the sample. This leads to longer measurement times in order to get the same information compared to transmission experiments.

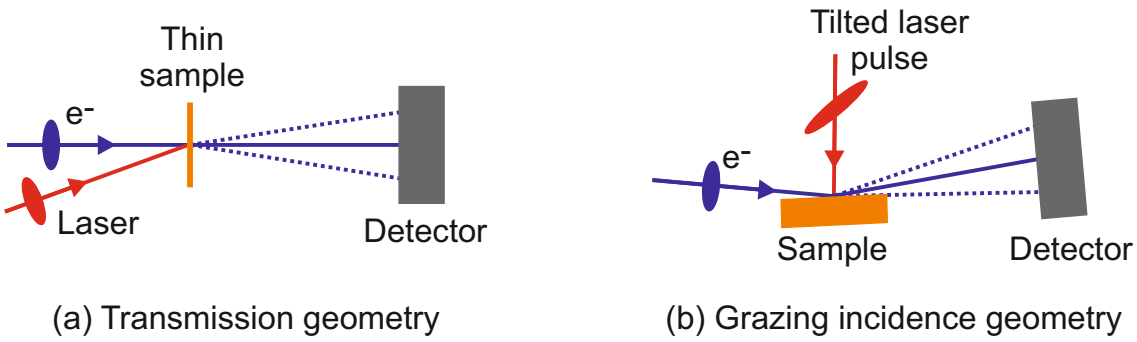

Figure 3.18: (a) Transmission and (b) grazing-incidence geometry for a time-resolved electron diffraction experiment.

In both cases you have the issue that electrons are not traveling with speed of light and therefore a velocity mismatch between the laser pump beam and the electron probe beam exists. In vacuum an electron moves with the velocity

$$v(E) = c\sqrt{1-(1+\frac{E}{m_e c^2})^{-2}}, \tag{3.7}$$

where E is the electron energy, m_e the electron's rest mass and c the speed of light. So, electrons with energies of 100 keV achieve only 0.548 c. This difference can lead to large blurring of time-zero, resulting in a severe limitation of the time resolution [110]. In order to reach the best time resolution, you have to take care that every point on the excited sample area "sees" the same delay between the pump and probe pulse, meaning that the surface velocities of the pump and probe pulses

must be equal. In transmission geometry, this can be easily achieved by choosing the angles between pump-, probe-beam and sample accordingly [69, 110]. For grazing-incidence, however, such a "close-to-collinear" arrangement is not possible. You can overcome this problem by using tilted optical pulses as described by Baum and Zewail in [111]. Figure 3.19 shows the concept. The laser pulse is such tilted so that its surface velocity matches the surface velocity of the electron pulse.

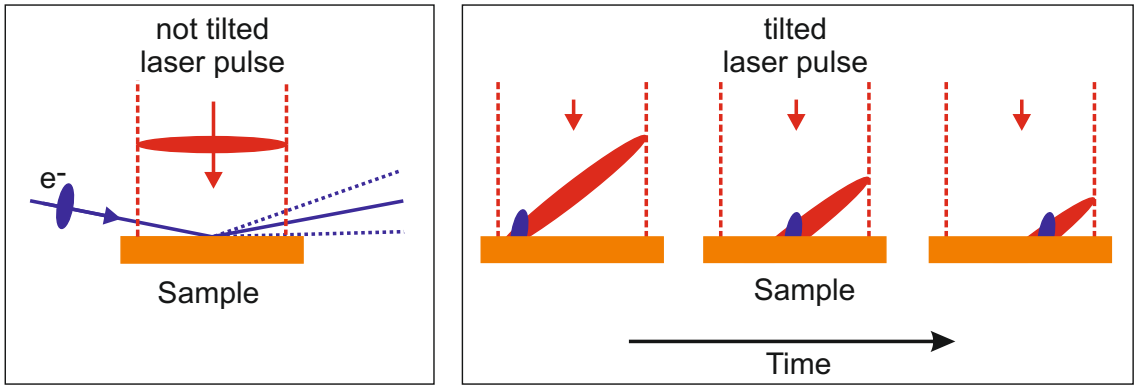

Figure 3.19: Laser excitation with not-tilted and tilted pulses in grazing-incidence geometry. The laser pulse hits the sample nearly perpendicular to the surface. Because of the velocity mismatch between the electron and laser beam, the time resolution is limited. To overcome this problem, tilted optical pulses are used, so that both the laser and electron pulses are coincident at every place on the specimen surface at all times [111].

Also in transmission geometry the use of tilted laser pulses can be practical if the velocity mismatch can not be compensated by an appropriate geometry, like it can be the case to fulfill an unfortunate Bragg condition. Either the laser pulse or the electron pulse can be tilted [69, 111].

So far, we have the following possibilities to excite the sample in our apparatus; with:

- the fundamental of our Yb:YAG thin-disk laser (cf. 2.2) at $\lambda = 1030\ nm$ and its second harmonic at $\lambda = 515\ nm$
- the output of the nonlinear optical parametric amplifier (NOPA) described in chapter 3.5, with tunable femtosecond pulses from $\lambda = 500\ nm$ to $\lambda = 700\ nm$
- THz radiation at a central frequency of 0.3 THz generated in a $LiNbO_3$ crystal as described by Schneider et al. in [36]

The specimen can be placed both in transmission and grazing-incidence geometry and tilted optical pulses can be applied.

3.8 Avoiding temporal distortions in tilted pulses

This chapter is a reprint of my publication in Optics Letters, Vol.37, No.12, June 15, 2012 [78].

Abstract: Tilted femtosecond laser pulses, having an intensity front with an angle to the propagation direction, can be generated by a dispersive element and a lens or mirror for imaging. Here we show that conventional geometries, for example with a grating at Littrow's condition, produce significant temporal distortions over the beam profile. The aberrations are the result of a mismatch between the grating's surface and the object plane of the imaging system. This changes the chirp of the pulses over the beam profile and lengthens the pulses to picoseconds for millimeter-sized beams. The distortions can be avoided by choosing a geometry in which the propagation direction of the tilted pulses is perpendicular to the grating's surface.

Tilted femtosecond pulses propagate with an intensity front that has an angle with respect to the direction of propagation. Incidence on a surface can produce a lateral sweep of the intensity that is slower than the speed of light. This is useful for providing group and phase matching in otherwise inaccessible geometries. Examples are the research fields of ultrafast electron diffraction [27, 111], x-ray lasers with traveling-wave excitation [112, 113], parametric amplification [114], or terahertz pulse generation [115–118].

Pulse front tilt is linked to angular dispersion [119–121]. A simple method for generating tilted pulses consists of a dispersive element (for example, grating) and an imaging system, which compensates for the undesired spatial separation of the different frequencies. The imaging system reproduces the tilted pulses at a location

in free space. There, all frequencies overlap at the same point, but come from different directions. For pulses at a central wavelength λ_0, the tilt angle γ is [121]

$$\gamma \approx \arctan(M \frac{\partial \theta_{out}}{\partial \lambda}\Big|_{\lambda_0} \lambda_0), \tag{3.8}$$

where $\theta_{out}(\lambda)$ is the angle of the grating's diffracted beam and M is the demagnification factor of the imaging system. For example, a grating with 2000 lines per mm used at Littrow's condition ($\theta_{in} = \theta_{out} \approx 53°$) produces tilted pulses with $\gamma \approx 70°$ after an 1:1 imaging system. Perpendicular incidence on a surface produces an effective group velocity of $\sim 0.37\ c$.

Most applications of tilted pulses require large beam diameters. In ultrafast diffraction, for example, the size of the beam determines the amount of surface to be excited. For terahertz generation, the pulse energy and beam diameter must be adjusted to achieve an optimized intensity for optical rectification. For x-ray lasers, the spot must be large for achieving efficient amplification of spontaneous emission. In addition, in all examples the pulses should have shortest duration and therefore require a large bandwidth. In these two regimes, femtosecond pulses and large beams, two effects become significant. First, Eq. 3.8 relates tilt angle and dispersion. One could therefore suspect that higher-order terms of the grating's dispersion may produce a nonlinear tilt, that is, "banana"-shaped pulses. Second, the grating induces temporal chirp [120]. The pulses become longer the farther they travel away from the grating; this is the mechanism of a grating compressor. The imaging system should reverse this chirp, but ray-tracing calculations predict a varying pulse duration at the target [122, 123]. Both effects can severely limit the applicability of tilted pulses.

In this Letter, we report an experimental study of nonlinearity and temporal distortions in tilted femtosecond pulses. Our measurement is based on recording a cross-correlation between a tilted and a non-tilted pulse. Figure 3.20 shows the setup. The laser source is a longcavity Ti:sapphire oscillator (Femtosource XL, Femtolasers GmbH), providing $\sim 60\ fs$ pulses at a central wavelength of $\lambda \approx 800\ nm$ with a repetition rate of 5.1 MHz and a pulse energy of $\sim 450\ nJ$. The collimated beam is separated into two parts by a 50% beam splitter (BS). One beam is guided through a cylindrical lens ($f = 300\ mm$) onto a grating; a linear focus with dimensions of $\sim 0.1 \times 5\ mm$ is achieved on the grating's surface (yz-plane). The first-order

reflection comes off closely to Littrow's condition; that is, mostly back toward the incoming beam. Going slightly upward (y-direction), the beam is steered onto a large spherical mirror ($f_{mirror} = 150\ mm$), which provides a 1:1 imaging of the field at the grating onto a β-barium-borate crystal (BBO) with a thickness of 100 μm. There, the beam has a size of $\sim 3 \times 0.1\ mm$ (xy-plane). The other 50% of the laser is used as a non-tilted reference. It is widened by a telescope, mechanically delayed and also cylindrically focused onto the BBO crystal, with a slightly larger size of $\sim 5 \times 0.1\ mm$ (xy-plane). The angle between the two beams is $< 4°$ and therefore negligible. With proper spatiotemporal overlap, sum-frequency generation provides a cross-correlation of the two incoming intensities.

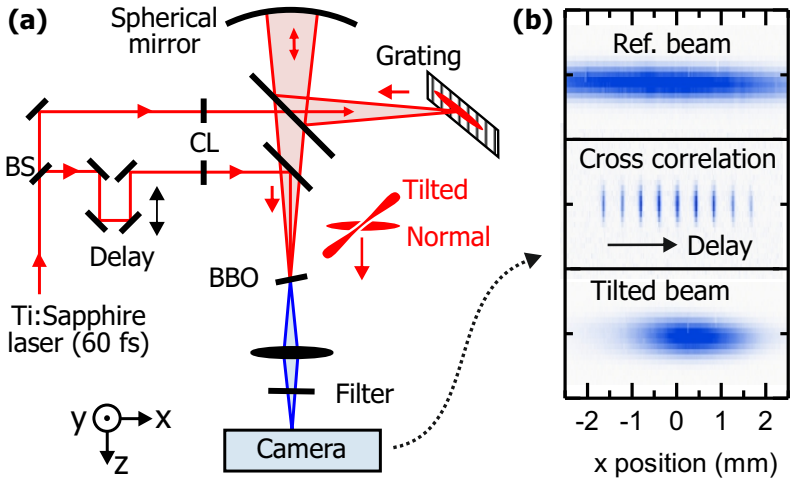

Figure 3.20: Arrangement for measuring the shape of tilted femtosecond pulses at 800 nm. (a) Experimental setup of a crosscorrelation between a tilted and a non-tilted pulse, where BS is a 50% beam splitter, CL represents cylindrical lenses, and BBO is a nonlinear crystal. (b) Pictures at 400 nm at the camera. Three contributions are produced: second harmonic of the reference beam (upper), second harmonic of the tilted beam (lower), and the cross-correlation signal for different delays (middle).

The purpose of the cylindrical focuses is to increase the intensity for nonlinear interaction. There are three contributions to the output at $\sim$ 400 nm: second harmonic of the tilted pulses coming from slightly above, second harmonic of the non-tilted pulses coming from slightly below, and a sum-frequency signal between the two. The output of the BBO crystal is imaged onto a camera (USBeamPro, Photon, Inc.). We applied a lens ($f = 60\ mm$) or a spherical mirror ($f = 200\ mm$)

with similar results. A spectral filter was used to suppress components around 800 nm and a slit was used to reject the two static contributions.

The cross-correlation signals are narrow strips, because sum frequency is only generated where the tilted and non-tilted pulses overlap in time; see depicted pulses in Fig. 3.20(a). Scanning the delay produces a sweep from left to right, which indicates the tilt. For each delay, we evaluated two parameters of the cross-correlation strips: central position and width. The positions provide a picture of the delay versus position, that is, the tilt. The widths provide the effective durations of the tilted pulse at all positions over the beam profile.

We used this arrangement to study two geometries for the diffraction grating. First, we applied Littrow's condition (input and output beams close to parallel), as shown in Fig. 3.21(a). This represents the geometry reported in the literature. We used a grating with 2000 $lines/mm$ and an incidence angle of 49°. The first-order beam exists at $\sim 58°$ and imaging with a magnification of ~ 1 provides an angular dispersion of ~ 3.7 $mrad/nm$, corresponding to an expected pulse front tilt of $\sim 71.5°$.

Figure 3.21(b) shows the results. The upper panel shows the delay versus position. We observed a straight line with a tilt of $\sim 71.9°$. No evidence for deviations from a purely linear tilt was found, although our 60 fs pulses have a considerable bandwidth (~ 30 nm). Higher orders of the grating's dispersion did not produce a curved shape of the pulses.

The linearity of the tilt over the entire beam profile can be understood by assuming causality at the grating's surface. Incidence of the incoming pulse "excites" the grating only during femtosecond times. The imaging system (the spherical mirror) reproduces this time-dependent intensity at the image location (the BBO crystal). Hence, the intensity profile at the BBO resembles a spatiotemporal image of the grating's surface. In this description, the tilt is linear because the grating is flat (not curved). Nonlinearities in the dispersion are not causing curved pulses, as shown here experimentally.

Measuring the pulse duration over the beam profile produced a less favorable result. The blue dots in the lower panel of Fig. 3.21(b) show what we measured with near-Littrow geometry. A strong lengthening is evident at the edges of the beam; the width of the cross correlation is ~ 1 ps at a position 1 mm away from the beam's center. This is too much to be acceptable in femtosecond experiments.

The mechanism is based on temporal distortions. Besides dispersing the pulses spatially, the grating also produces a temporal chirp; this lengthens the pulses the more they travel away from the grating [120]. The spherical mirror reverses the angular and the temporal dispersion. At the image (the BBO crystal), the pulses should therefore be short again. It is indeed the case at the beam center, where the distances D_{gr} (between grating and spherical mirror) and D_{BBO} (between spherical mirror and BBO) provide an imaging condition ($1/f_{mirror} = 1/D_{gr} + 1/D_{BBO}$). However, the grating is tilted with respect to the direction of the first-order beam. The imaging system's object plane (horizontal dotted line) has an angle θ_{out} with respect to the grating. Imaging is, therefore, imperfect for outer parts of the beam. The spherical mirror (or lens) is not fully reversing the temporal dispersion, and the pulses become chirped.

In order to calculate this, we invoke the geometry depicted in Fig. 3.21(a). At a lateral distance Δx from center, the distance D_{gr} is increased/reduced by $\Delta z = \Delta x \cdot \tan(\theta_{out})$. At a distance Δz from the grating, a pulse with a Fourier-limited duration τ_0 acquires a duration $\tau(\Delta z)$ that is given by [120]

$$\tau(\Delta z) \approx \tau_0 \sqrt{1 + \frac{(2\ln 2)^2 \Delta z^2 \psi^4 \lambda_0^6}{\pi^2 c^4 \tau_0^4}}. \tag{3.9}$$

This is Eq. (23) of [11], rewritten for an angular dispersion $\psi = M \cdot (\partial\theta_{out}/\partial\lambda)|_{\lambda_0}$ in wavelength units (rad/nm), and for pulse durations defined by full width at half maximum. Contributions originating from the spatial separation of the frequencies are neglected, because our beams are large in the plane of diffraction.

We also account for the apparatus function of our cross-correlation setup. Our camera has a pixel size of 6.7 μm, corresponding to a temporal resolution of $\tau_{camera} \approx 6.7\ \mu m \cdot \tan(\gamma)/c \approx 70\ fs$, as a result of the lateral sweeps of the cross-correlation signal over the camera. The duration of the non-tilted pulses is $\tau_0 \approx 60\ fs$. Considering these effects, the measured cross-correlation width is $\tau_{cross} \approx \sqrt{\tau(\Delta z)^2 + \tau_0^2 + \tau_{camera}^2}$. Compared to $\tau(\Delta z)$, this makes a slight difference only at very short durations of $\tau(\Delta z)$.

The red line in the lower panel of Fig. 3.21(b) shows the results. A good agreement to the experimental data is evident. It shows that the discrepancy between

the grating and the imaging plane is indeed the reason for the observed temporal distortions and "bone"-shaped pulses at the target.

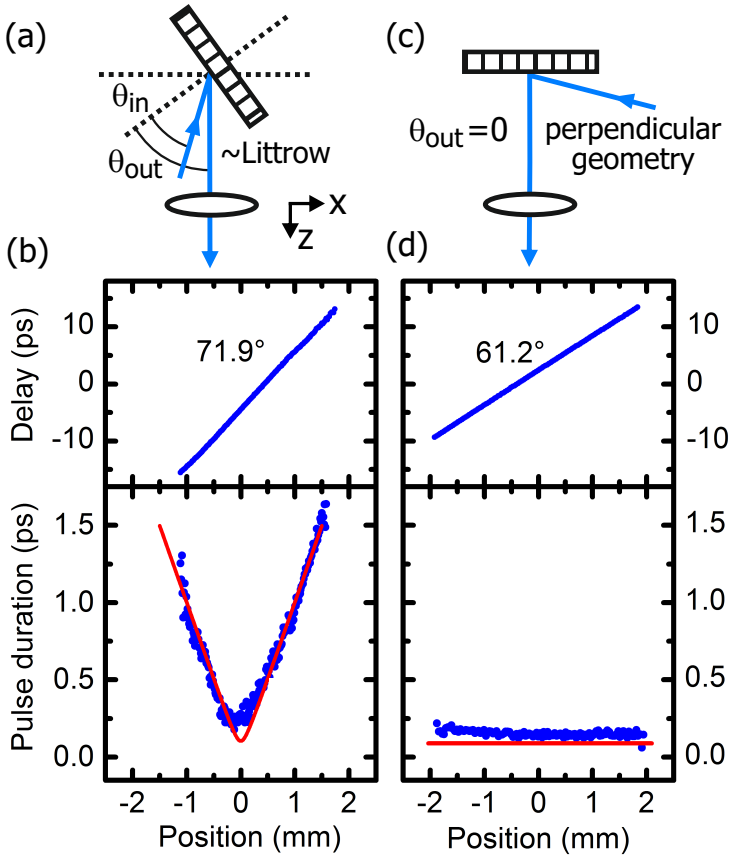

Figure 3.21: Temporal distortions in tilted pulses for two different geometries of the grating. (a) Conventional arrangement with a Littrow grating. (b) Resulting pulse front tilt (upper panel, blue) and pulse duration (lower panel, blue) in dependence of the position within the beam. The red line is a calculation (see text). (c) Geometry to avoid aberrations, based on a perpendicular exit of the diffracted beam. (d) Resulting pulse front tilt (upper panel, blue) and pulse duration (lower panel, blue). The red line is a calculation.

From these results it is evident how to avoid such aberrations. Coincidence of the grating with the object plane of the spherical mirror is required; the diffracted beam must exit the grating in a perpendicular direction. This principle was identified earlier [124]; here we provide a measurement with femtosecond pulses. Figure 3.21(c) depicts the geometry. In the experiment, we used a grating with 1100 $lines/mm$, an incidence angle of 61.5°, and a demagnification of $\sim 1:2$ ($D_{gr} \approx 450\ nm$ and

$D_{BBO} \approx 225\ nm$). The expected pulse front tilt is $\sim 60°$ in such a configuration. The grating's blaze and efficiency were not optimized for these angles; this will be a challenge for the future. Figure 3.21(d) shows the results. The tilt is linear, as expected from our grating's flat surface. In contrast to conventional geometry, the pulse duration is short over all of the beam profile (Fig. 3.21(d), lower panel). The prediction by Eq. 3.9 for $\theta_{out} = 0$, convoluted with the experimental resolution, produces the red trace. Theory deviates only slightly from the measured data. This shows that temporal distortions in tilted pulses can be avoided by choosing a geometry where the grating lies on the imaging system's object plane.

To generalize, the grating's angle θ_{out} determines the plane where the pulses are compressed. The combination of θ_{out}, θ_{in}, and M determines the pulse front tilt. In an application, both planes can be set as required by the sample's position and orientation. The depth-of-field of the imaging system defines the amount of temporal distortions.

We note some consequences of these results. First, in the field of intense terahertz generation, large beams are required to balance intensity and pulse energy [125]. A contact grating was proposed to minimize distortions [122]. In view of our results, an appropriate tilt of the grating also might be as successful. Second, in the field of x-ray lasers, traveling waves can be delivered to large targets with femtosecond duration everywhere. This opens up the possibility to use few-cycle petawatt lasers [126] for producing coherent x-ray beams. Third, in the field of ultrafast electron diffraction, temporal resolution in grazing incidence is essentially unlimited by velocity problems. If using single electrons [21], compression in microwaves or ponderomotive gratings [6, 28], ultrashort laser pulses at megahertz repetition rates [127], and suitable arrangements for tilt, the regime of few-femtosecond resolution is in range.

4 Time-resolved few-electron diffraction on carbon nanotubes

Here I describe the first time-resolved electron diffraction experiment made with this apparatus. The high 100-kV acceleration voltage allows to study thick and complex solid samples. As a sample, a 200-nm thick foam consisting of carbon nanotubes was chosen. Carbon nanotubes' dynamics are very interesting both from a technological and a fundamental perspective. The dynamics of the carbon-nuclei are not yet understood well [128] and ultrafast electron diffraction provides an ideal tool to observe these dynamics. Therefore, the carbon nanotube film is an ideal sample to use for a proof-of-principle experiment for the new "UED2-beamline".

4.1 Motivation

Since the discovery of carbon nanotubes (CNTs) in 1991 by Sumio Iijima [129], they keep drawing attention of many scientists in different research fields due to their unique properties in optics [130–132], mechanics [133], electrical as well as thermal conductivity [134, 135] and electronics [136]. Carbon nanotubes consist of cylindrical rolled-up graphite layers and individual walls behave as metals or semiconductors, depending on their chirality [137], i.e. the orientation of the lattice. Figure 4.1 shows an illustration of a single-walled carbon nanotube.

Carbon nanotubes combine some of the best features of polymers, carbon fibers and metals [138] and are thus an ideal multifunctional material useable for many applications [139]. They can be produced nowadays in macroscopic quantities and applications, like nanotube diodes [140], sensors [141, 142] and even a computer built entirely out of CNT-based transistors [143] were already successfully demonstrated.

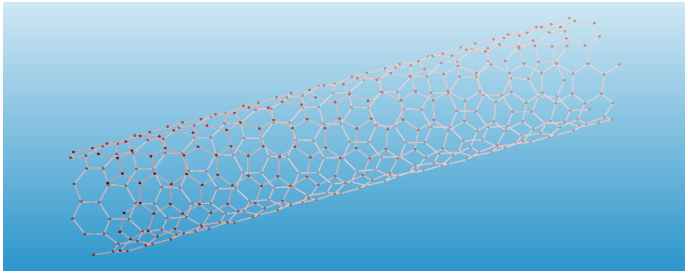

Figure 4.1: Illustration of a single-walled carbon nanotube. A single-walled carbon nanotube consist of a graphene sheet rolled up to a cylinder. The picture was generated with Crystal Maker.

Furthermore, carbon nanotubes have even been proposed as the climbing cable for a supposed future space elevator [144] due to their high strength-to-mass ratio.

Carbon nanotubes' ultrafast characteristics have been investigated using a wide array of measurement-methods. E.g., the dynamics of charge-carriers in carbon nanotubes were studied using ultrafast spectroscopy [145], or specific vibrational modes were observed by Raman spectroscopy [146]. These techniques, however, provide only an indirect measurement and are not capable to study directly time-dependent atomic motion. In carbon nanotubes the dynamics of the carbon-nuclei, however, are not yet understood well [128], and time-resolved electron diffraction provides an ideal tool to address these dynamics.

4.2 Sample preparation

Freestanding films of carbon nanotubes with $\sim 200\ nm$ thickness were provided by Wenjun Ma and produced by direct synthesis, similar to the procedure described in [147]. The films were grown by floating-catalyst chemical vapor deposition (FC-CVD), where as catalyst a ferrocene/sulfur powder is heated up to $\sim 358\ K$ and then streamed into a reaction zone by $\sim 592 \cdot 10^3\ Pa\ m^3/s$ argon and $\sim 2 \cdot 10^3\ Pa\ m^3/s$ methane [147]. The reaction in the quartz tube was carried out at over $875\ K$ and large-area carbon nanotube films are grown there with a rate of $\sim 3\ nm/min$ [147].

With this method, huge robust freestanding foils can be produced, as shown in figure 4.2(a). The carbon nanotube film is macroscopically very homogenous but microscopically complex, as one can see in a large-scale scanning electron microscopy (SEM) image (figure 4.2(b)) kindly provided by Wenjun Ma. In the foil, the single

carbon-nanotubes form bundles, which are not randomly distributed, but preferentially aligned with respect to the flow in the reaction zone during the growing-procedure [147]. Furthermore, the bundles are firmly connected to each other; this results in a very high tensile strength of the film of about 360 MPa (along the preferential direction) [147]. In addition, the film has along this preferential direction an electrical conductivity of over 2000 S/cm [147], similar to the electrical conductivity in graphite parallel to the basal plane. The 200-nm thick film has a density of ~ 1.3 g/cm^3 [147] which is by a factor of ~ 1.7 lower compared to graphite.

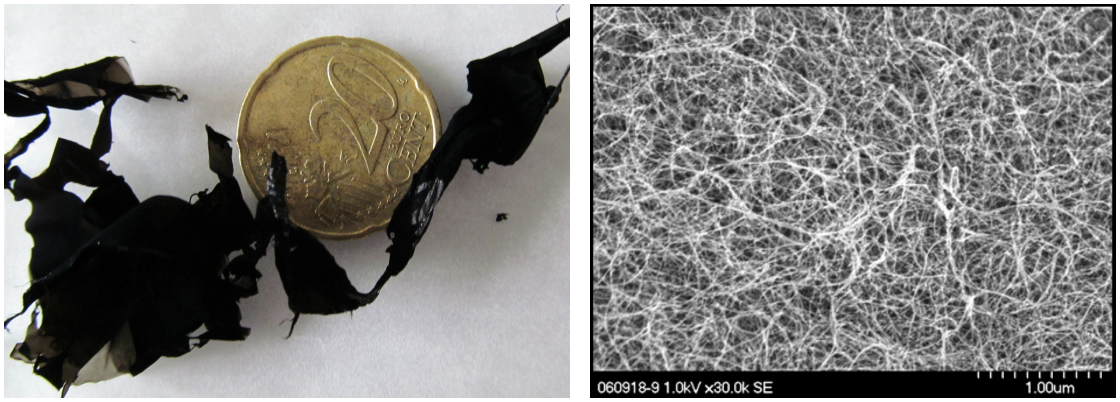

Figure 4.2: (a) Photograph of a ~ 200 nm thick freestanding carbon nanotube foil besides a 20-cent coin. (b) Scanning electron microscopy (SEM) image of the carbon nanotube film. The image was kindly provided by W. Ma and shows a high homogeneity of the sample.

For ultrafast electron diffraction investigations, the foil was attached to 2000-mesh copper TEM-grids (G2786C, plano GmbH) that are mounted on a home-built sample holder. Transmission electron microscope grids (TEM-grids) are commonly used to mount samples in electron microscopy and consists of very thin bars orientated in a mesh-like raster. The here used TEM-grid has 2000 bars per inch, with a bar thickness of ~ 5 μm [148]. The TEM-grid stabilizes the sample mechanically, but more important in our case, it provides efficient heat-sinks for removal of laser energy as discussed in chapter 4.4. Figure 4.3 shows a microscopy image of the carbon nanotube film mounted on such a TEM-grid.

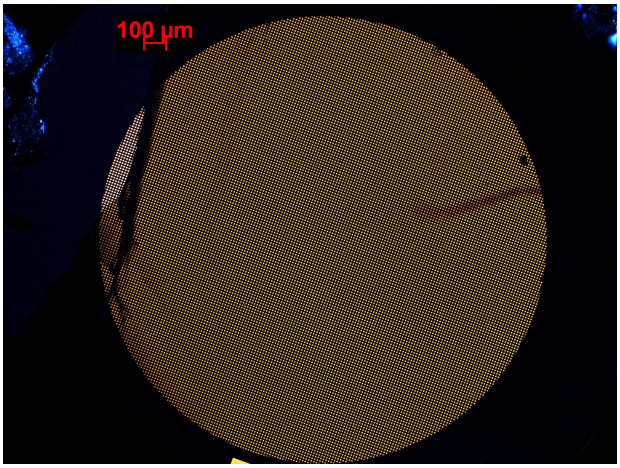

Figure 4.3: Microscopy image of a 200 nm thick carbon nanotube foam on a 2000 mesh TEM-grid. The TEM-grid provides efficient heat-sinks for support and continuous removal of laser energy.

4.3 Experimental parameters

The pump-probe experiment was carried out at an electron acceleration voltage of 100 kV and repeated at 91 kV. The laser repetition rate was set to its lowest value of 50 kHz and electron pulses with roughly 10 electrons/pulse were generated using the second harmonic of the laser-system (cf. chapter 2.2). The magnetic lens was aligned as described in chapter 3.4. The sample was excited with the fundamental laser pulses at 1030 nm. Because of the rather long pulse duration ($\sim 1\,ps$) the use of single-electron pulses is not so critical, and the here applied ~ 10 electrons per pulse do not limit the time resolution in this experiment. If in the future shorter pump pulses would require truly single-electron pulses, one could increase the repetition rate of the laser in order to keep the measurement time equal.

4.4 Determination of the optical damage threshold

In order to trigger the maximum excitation effect in the carbon nanotube foil, one has to know how much energy can be deposited there with the laser pulses without damaging it. So it is crucial to know the power threshold before irreversible damage occurs.

Earlier evidence [23] shows that sample damage in few/single-electron UED typically occurs not by the excitation of each individual laser pulse itself but by the average power over many pulses. For single- or few-electron diffraction experiments, the sample has to withstand many pump-probe cycles due to the long measurement time caused by the low intensity of a single diffraction image. The heating up of the sample and finally melting or sublimation is believed to be the main source of destroying the films. Therefore sufficient heat-sinks have to be provided in order to avoid thermal damage [23, 24]. The use of appropriate TEM-grids with a small mesh bar spacing as sample mounts proofed very beneficial to remove heat [23]. Damage measurements on 50-nm thin aluminum foils mounted on different TEM-grids show that one can increase the damage threshold by a factor of 10 by increasing the number of bars per inch from 100 to 2000 [24].

For simplicity we used the fundamental of our laser system (1030 nm) to optically excite the sample. At 1030 nm, the transmission of the carbon nanotube foam is 71%. This high transparency (see also figure 4.3) is another indication that our films are very homogeneous and that impurities are at a low level [147]. Because of the high transparency of the films, it was not so easy to determine the threshold in situ with good resolution by only measuring the change in transmission. Therefore the foils were carefully examined by a light microscope after exposures to a set of different excitation energies. The measuring procedure was the following: We set the laser power to a certain value, focused it exactly like in the pump-probe experiment on the sample (40 μm beam width FWHM, ~ 1 ps pulse duration at 1030 nm central wavelength) and exposed the foil for ~ 5 min. Then we blocked the laser, moved the sample by 250 μm and repeated the measurement. For each laser power we exposed the foil at 6 different spots to assure that no local inhomogeneities, impurities or bad contacts to the TEM-grid would falsify the results. Finally, we expected the foil for visible damage under a bright field light microscope (Carl Zeiss, Axio Imager Z1m) using transillumination.

Figure 4.4 shows the results. The laser power was changed in 0.5-mW steps from 6 to 9.5 mW at a laser repetition rate of 50 kHz. First visible damage occurs at 8 mW; at a laser power above 8.5 mW all spots were destroyed. For the pump-probe experiment the excitation was therefore set to 7 mW (pulse energy 140 nJ), in order to have a safety margin. With the focus size of 40 μm beam width (full width at half maximum) this accords to a fluence of ~ 10 mJ/cm^2.

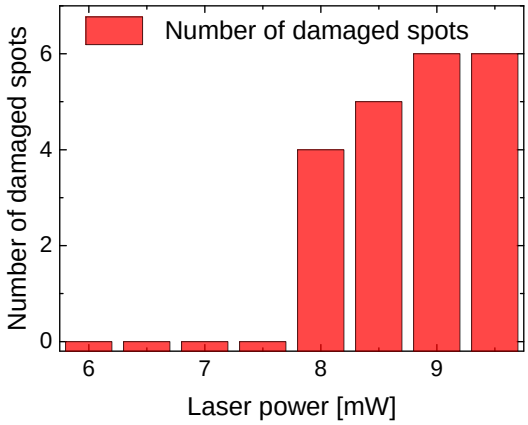

Figure 4.4: Optical damage threshold of the carbon nanotube foil mounted on a 2000 mesh TEM-grid. The foil was exposed $\sim 5\ min$ at six different spots for each laser power and then microscopically examined for damage. The repetition rate was 50 kHz, pulse duration $\sim 1\ ps$, wavelength 1030 nm and spot size on the foil 40 μm diameter (full width at half maximum).

4.5 Pump-probe: overlap of the laser with the electron-beam

For pump-probe experiments it is essential to overlap the pump with the probe beam both spatially and temporally on the sample to investigate. First, the temporal overlap (the so called time-zero) is addressed; then a procedure to exactly overlap the focused beams in space is discussed.

In order to perform an ultrafast electron diffraction experiment in a reasonable time frame, one has to choose the range and sensitivity of delay times appropriately, which requires to know when the two pulses coincide in time. The tuning of different delay steps is provided by a retroreflector placed in the laser beam and mounted on a linear delay stage (LS110, PI miCos GmbH) with a travel range of 305 mm; hence covering a time interval of $\sim 1\ ns$ with a step size better than 0.5 fs[149]. First, a precise measurement of the length of the two beam paths is performed to know roughly where time zero shall be, taken into account that electrons are not traveling with the speed of light, and that the velocity depends on their energy (equation 3.7). Therefore, if one changes the acceleration voltage of the electrons, one has also to adapt the optical beam path. Next, the TEM-grid covered with the carbon nanotube

film to investigate (cf. figure 4.3) is placed with the sample positioning system (see chapter 3.6) in the unfocused electron beam. The electrons produce a shadow image of the sample and you focus the electron beam slightly so that it homogeneously illuminates the TEM-grid with the specimen. Then one brings the focused laser beam to the TEM-grid and increases the intensity so much that it burns a hole in the specimen, but not in the TEM-grid; note that the fundamental of the laser ($\lambda = 1030\ nm$) is visible with the camera described in chapter 3.6. Now, the electron and laser beam are roughly overlapped in space. On the sharp edges of the grid, the intense laser pulse generates photo-electrons by multiphoton photoemission that deflect the electron pulse by space charge effects, if the timing is appropriate. So by recording the electron beam shape at different delay steps, a deflection of the electron beam at time zero is detected.

For the determination of time zero, t_0, six time-scans were performed and the resulting images for each time step averaged. Since we are only interested in the change of the charge distribution, an averaged reference image at a time position $t_{ref} \ll t_0$ is subtracted from the other images to increase contrast. Figure 4.5 presents the results. A deflection of electrons is clearly visible at time zero. Figure 4.6 shows the absolute change in the integrated intensity profile with time; in order to increase the resolution we used the squared differential intensities [25]

$$\Delta I(t) = \sum_{i,j} [I_{i,j}(t) - I_{i,j}(t_{ref})]^2, \tag{4.1}$$

with $I_{i,j}$ the pixel values.

This deflection effect last for $\sim 40\ ps$, so to find t_0, one can perform a fast rough scan first and then make a fine scan around t_0 to determine it more precisely. With this method we can resolve time zero within $\pm 1\ ps$. We note that this procedure is efficient enough to set the delay steps in our current experiment appropriate, but in order to determine t_0 with femtosecond precision one has to perform cross-correlation measurements, for example described by Kirchner et al. in [68].

The two beams are now aligned roughly in space, but to accomplish a successful pump-probe experiment their focuses have to match exactly, otherwise a mixture of diffraction patterns of excited and not excited areas is measured. The focus of the electron beam on the sample was determined by knife-edge scans and has a diameter of $\sim 32\ \mu m$ (FWHM). The size of the pump beam was set to $\sim 40\ \mu m$;

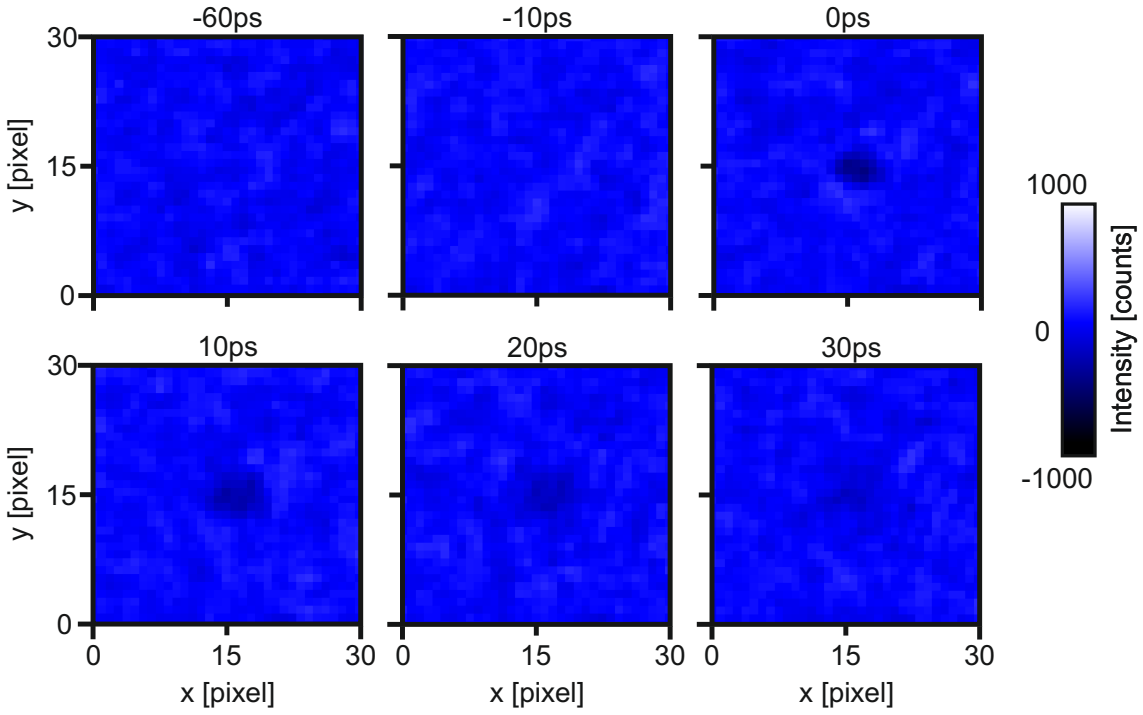

Figure 4.5: Procedure to find the temporal overlap between the electron and the laser pulse. The laser pulse generates photo-electrons leading to a charge distribution deflecting the electrons of the electron probe beam. Thus time zero can be determined by recording the electron beam profile at different delay steps.

slightly larger in order to record only diffraction patterns from the excited area as mentioned above. To overlap the two beams in space, we burned a tiny cross with the laser in the carbon nanotube film and performed knife-edge scans their with the electron beam. Thus the electron beam and the laser can be exactly overlapped in the middle of the cross. To check if the procedure was sufficient, we block the laser beam and move the sample by some 100 μm. Then we increase the electrons per pulse and the exposure time of the detector such that the diffraction pattern is clearly visible. If one burns now a hole with the laser, the diffraction pattern has to disappear completely.

Next, the sample is moved again by some 100 μm, such that the beams are in an undamaged region of the sample. Now the time-resolved diffraction experiment can be performed. We note that the weak laser power of 7 mW used for excitation

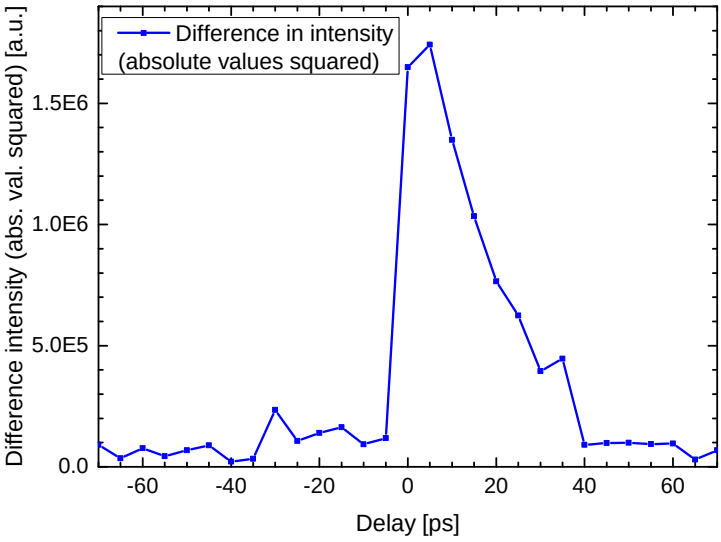

Figure 4.6: Determination of the temporal overlap between the electron and the laser pulse. The absolute values of the intensity are squared in order to increase the sensitivity. For further details, see text.

produces not enough photo-electrons on the carbon nanotube sample to deflect our electron-beam and the correspondent diffraction pattern in any noticeable way.

4.6 Carbon nanotube diffraction and radial data analysis

Figure 4.7 shows an averaged diffraction pattern of the carbon nanotube sample resulting from 40 images with a 30-s exposure time, recorded at an electron energy of 100 keV at a time well before time zero. About 10 electrons per pulse at a repetition rate of 50 kHz were used. There are approximately 10^7 single electrons in this total pattern.

For evaluation of the diffraction rings, the averaged images were transformed into elliptic polar coordinates, angularly integrated and the values of the radius in pixels converted to reciprocal distances. Elliptic coordinates have to be used because the recorded diffraction rings are not perfectly circular, but show a slight ellipticity,

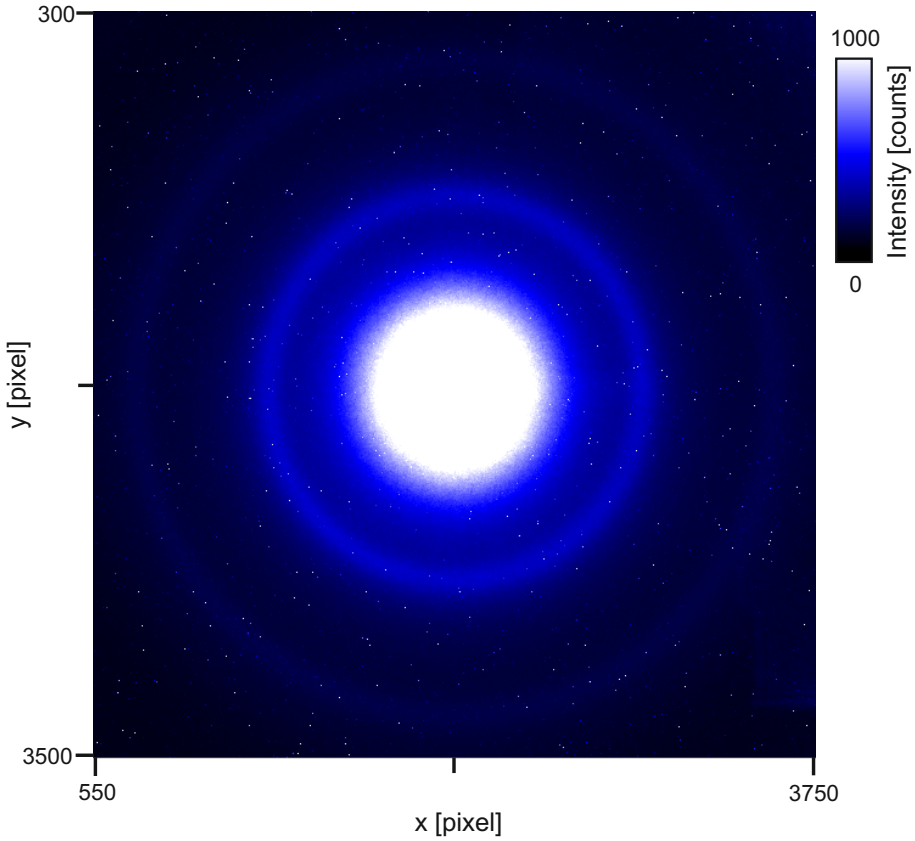

Figure 4.7: Diffraction pattern of the carbon nanotube film recorded at an electron energy of 100 keV. The picture results from the average of 40 images whereat the exposure time of the camera was set to its maximum value of 30 s.

resulting from an imperfect alignment of the camera to the electron beam. The transformation from the detector coordinates (u, v) into the elliptic polar coordinate system (r, ϕ) is described by

$$r = \frac{L\sqrt{(u-u_0)^2\cos^2\alpha + (v-v_0)^2}}{L - (u-u_0)\sin\alpha} \tag{4.2}$$

$$\phi = \arctan 2(u-u_0, v-v_0), \tag{4.3}$$

with L the distance from the sample to the detector and α the tilt angle of the camera with respect to the electron beam. To determine the tilt angle α we used a computational optimization algorithm based on minimizing an objective function,

resulting in a tilt of $\alpha \approx 4.6°$. The same algorithm was also used to find the ring center, i.e. the (000) order, and set it as the point of coordinates' origin u_0, v_0.

The green trace in figure 4.8 shows the results. Up to four rings are clearly evident. This demonstrates the ability of our "UED2" apparatus (cf. chapter 3) to measure complex, thick materials.

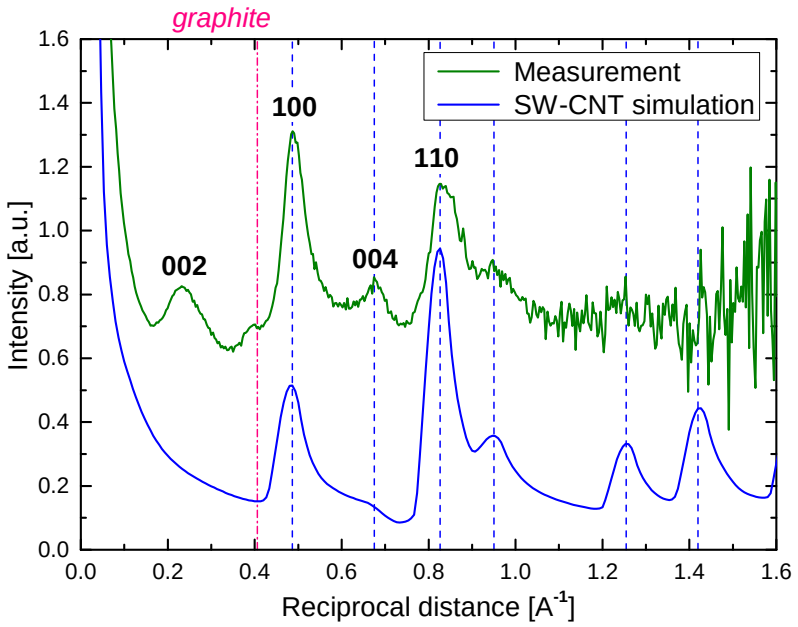

Figure 4.8: Angular integrated diffraction pattern of the recorded diffraction image (green trace) and of the simulation of a SW-CNT (blue trace). Peak assignments are also shown and the pattern indicates that our CNT-film consists of a mixture of SW-CNTs and MW-CNTs.

With help from P. Baum, a simulation of the diffraction pattern from a single-walled carbon nanotube (SW-CNT) was performed following the mathematics of Lu-Chang Qin in [150], radially averaged and averaged over different chiralities. The result is plotted in figure 4.8 (blue trace). The 100 and 110 peak can be associated with the covalent bonds in the graphene sheets (intra-tubule) [128, 151] and show a good agreement with the simulations. The 002 and 004 peak refer to diffraction by inter-tubule planes [128], i.e. by adjacent graphene planes in multi-walled carbon nanotubes (MW-CNT) [151]. The lower intensity of the 00l peaks with respect to the 100 and 110 peak indicates that our carbon nanotube film consists of a mixture

of SW-CNTs and MW-CNTs, where the MW-CNTs are likely composed of only a few walls [152].

4.7 Time-resolved results and discussion

For the time-resolved studies we recorded 40 diffraction images with 30 s exposure time at every time-step, corresponding to roughly 10^8 incoming electrons for the averaged image per time-step. The 002, 100, and 110 diffraction peaks were fitted using a Gaussian function to determine their positions. Two measurements were performed, one at an electron energy of 100 keV and one at 91 keV. These measurements show reasonably similar results and therefore, the dynamics of the two measurements were averaged. Figure 4.9 shows the change in position of the peaks with time.

The dynamics were fitted with a Gaussian-convolved step function (assuming that the laser and electron pulses have Gaussian profiles) followed by an exponential decay described by

$$y = y_0 + \frac{1}{2}af(t - t_0, r, \tau) + \frac{1}{2}bf(t - t_0, r \to \infty, \tau) \tag{4.4}$$

with y_0, a, b offsets and amplitudes, respectively, r the decay-rate and τ the apparatus' temporal resolution (full width at half maximum(FWHM)); assuming that the dynamics fitted with the error-function are faster than the time duration of the excitation pulse, τ can be associated with the time resolution of the experiment. The function f is given by

$$f(t - t_0, r, \tau) = \exp[(\frac{\tau}{4r\sqrt{\ln(2)}})^2 - \frac{t - t_0}{r}](1 - \mathrm{erf}[\frac{\tau}{4r\sqrt{\ln(2)}} - \frac{2(t - t_0)\sqrt{\ln(2)}}{\tau}]). \tag{4.5}$$

The fit of the 100 peak (figure 4.9(b)) unfolds a time resolution of $\tau = 1.6$ ps (FWHM). With a laser pulse duration of ~ 1 ps this result is quite reasonable. Since the measurement-data of the 100-dynamics are less noisy compared to the two other data-sets the time resolution τ was set constant for all fits. Table 4.1 shows

the results with y_0 (change before time-zero) and t_0 (time-zero) already corrected to zero (cf. figure 4.9).

	002-fit	100-fit	110-fit
τ (fixed)	1.6 ps	1.6 ps	1.6 ps
r	7.9 ps	8.2 ps	7.1 ps
a	1.43 ‰	-0.23 ‰	-0.31 ‰
b	$b = -a$	-0.25 ‰	0.04 ‰

Table 4.1: Fit-parameters of the carbon nanotube dynamics. For details, see text.

The exponential fit of the 002 peak dynamics results in a time-rate of $r_{002} = 7.9\,ps$. The time-rates of the 100 and 110 peaks are also in the same range, $r_{100} = 8.2\,ps$ and $r_{110} = 7.1\,ps$. The fit parameter b is the offset at 50 ps with respect to the zero-position. After 50 ps the 002 peak is shifted by $b_{002} = -1.43$ ‰, the other peaks by $b_{100} = -0.25$ ‰ and $b_{110} = 0.04$ ‰, respectively. a describes the amplitude of the exponential function and equals $a_{100} = -0.23$ ‰ and $a_{110} = -0.31$ ‰, respectively.

These results allow a preliminary interpretation of the atomic-scale dynamics of carbon nanotubes after laser excitation. We draw on previous knowledge of graphite, where after exposure with an ultrashort laser pulse, the excited carriers gain a local equilibrium in some hundred femtoseconds by transferring heat to a subset of strongly coupled optical phonons (SCOPs) [24, 153]. In graphite, the SCOPs have a life-time of $7 - 12\,ps$ [153–155], before they have transferred their energy into other modes.

The time-rates r in the carbon nanotubes match quite well the time scale of the SCOPs in graphite. In the carbon nanotubes, after laser excitation, the energy is probably transferred in less than the time resolution (1.6 ps) to SCOPs and the tubes are almost instantly thermally expanded (see figure 4.10). The 002 peak, representing the distance between the walls of multi-walled carbon nanotubes, shows not such a fast dynamic, meaning that the smaller carbon nanotubes are equally expanded as their neighboring larger ones. Within $\sim 8\,ps$ the SCOPs probably thermally relax back to an equal energy deposited in all modes. The tubes contract, whereas the effect is faster for smaller carbon nanotubes, evident from the increasing distance between the tubes (see figure 4.9(a)). This assumes that the carbon nanotubes are not completely ringlike after the decay of the SCOPs, but rather in a deformed vibrational state.

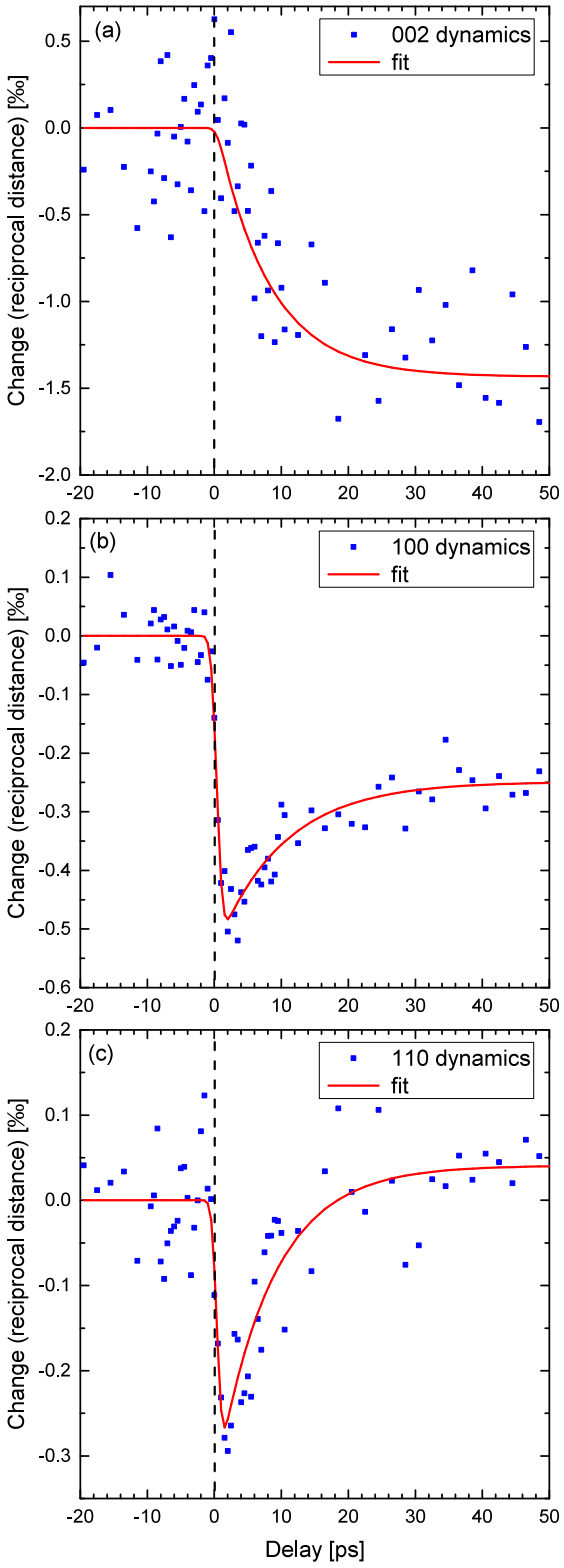

Figure 4.9: Dynamics of the CNT-film. Temporal behavior of different diffraction-peaks, measurement (blue) and fit (red). For details, see text.

At 50 *ps*, the end of the here investigated time range, the tubes are still radially expanded. This result agrees to measurements on the nanosecond to microsecond timescale performed by Park et al. in [128]. They observed a radial expansion which lasts several microseconds [128]. The total recovery time was found to be about 100 μs [128], governed by thermal conductivity laws.

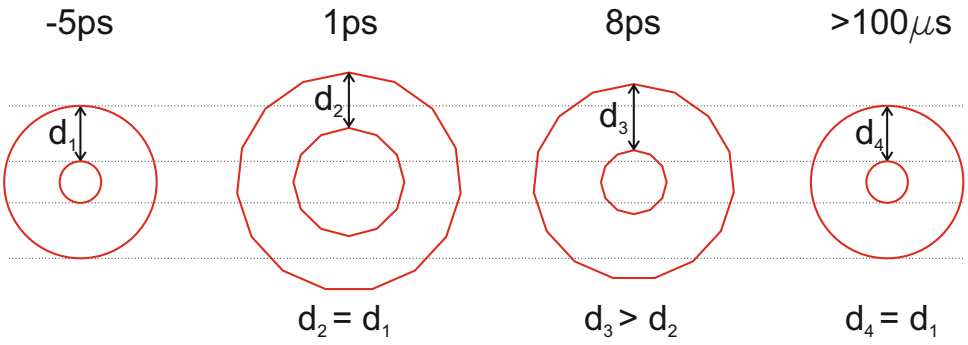

Figure 4.10: Schematics of the carbon nanotube dynamics, here shown for a carbon nanotube (CNT) with 2 walls. After ultrafast laser heating (1*ps*) the CNTs are thermally expanded. The smaller CNT is equally expanded as the larger one and the radial distance between them remains constant ($d_2 = d_1$). Within $\sim$ 8 *ps* the system thermally relaxes and the tubes contract, whereas the contraction is larger for the smaller CNT, meaning that the distance d is increasing ($d_3 > d_2$). After this relaxation, the CNTs are still radial expanded compared to the not-excited state (-5 *ps*). Measurement performed in [128] show, that it takes $\sim$ 100 μs to reach the not-excited state. For further details, see the text.

The offsets b of the 100 and the 110 position may eventually results from the chirality of the carbon nanotubes, meaning the orientation of the graphene lattice with respect to the tube radius. We assume that most of the carbon nanotubes have such chiralities where the 100 peak represents the equatorial dimension; this would confirm the radial expansion. Park et al. could only observe a shift in the 002 peak and argued that their nanotube structure is scroll-type [128]. Our measurement, however, shows clearly a shift in the 100 peak, indicating a system of closed carbon nanotube rings, which is more likely [152].

The positive offset at 50 *ps* of the 110 peak-position is not a priori clear. If the 110 diffraction represents the axial direction, this would indicate a contraction along the tube axis. This is very unlikely and would mean that the carbon nanotubes have

a negative axial expansion coefficient. The offset of the 110 peak-position is not yet understood well; further measurements or simulations are required.

We conclude that after ultrafast laser heating, carbon nanotubes quickly thermally expand and then relax in $\sim 8\ ps$, the typical time-rate observed also in graphite dynamics. After this relaxation, the carbon nanotubes reach a thermal equilibrium, whereas they are radially expanded compared to the not-excited state, with larger tubes remaining more expanded than smaller ones. This anisotropic behavior can be associated with the difference in the bonding structure. Typical time-scales to again reach the non-excited state are in the order of microseconds [128].

Further studies, for example in dependence of laser fluence or polarization, or measurements with better time resolution can shed more light on the rich ultrafast ongoings in carbon nanotubes. Here, the experiment is a clear proof that ultrafast electron diffraction with single- or few-electron-pulses at 100 keV is a valuable and powerful tool, thanks to the improvements and findings made in this thesis, for investigating complex materials' dynamics in space and time.

5 Conclusion and Outlook

In this work, a new laboratory was established, housing a second-generation ultrafast electron diffraction beamline, "UED2". In comparison to before, the electron acceleration voltage was increased from 30 kV to 100 kV, in order to have a larger electron penetration depth, allowing in transmission geometry the use of much thicker samples. Grazing-incidence diffraction can also be applied. To minimize temporal distortions, the generation and characterization of appropriate optical tilted pulses was demonstrated. Furthermore, temporal distortions caused by misaligned magnetic lenses were examined and an alignment procedure to minimize the aberrations to less than one femtosecond is shown.

The stability of the 100-keV electron source is well sufficient for days of averaging. This allowed a first proof-of-principle experiment with this novel diffraction beamline. Carbon nanotubes were found to have a very rich and complex structural dynamic, covering multiple dimensions and time scales. This demonstrates that ultrafast electron diffraction at 100 keV, with single/few electrons per pulse, is an excellent method to study dynamics in complex solid samples in space and time.

When these results are combined with other activities in our group, the goal to reach few-femtosecond or even attosecond time-resolution in UED comes within reach. By compressing the single-electron pulses with microwave fields, pulse durations of only 28 fs (full width at half maximum) were already achieved [31, 32]. According to simulations [28], this concept promises attosecond capabilities. Another very promising concept is the compression with optical fields, and just now the "UED2-beamline" is upgraded to house such a compression. Combining these concepts will potentially push the limits in UED significantly further to complex materials and ultimate time-resolutions.

Bibliography

[1] P. Read and M. P. Meyer. *Restoration of Motion Picture Film*. Elsevier Science, 2000.

[2] E. J. Muybridge. The horse in motion. *Library of Congress Prints and Photographs Division; http://hdl.loc.gov/loc.pnp/cph.3a45870*, [online accessed October 07, 2014].

[3] L. Gao, J. Liang, C. Li, and L. V. Wang. Single-shot compressed ultrafast photography at one hundred billion frames per second. *Nature*, 516(7529):74–77, December 2014.

[4] T. H. Maiman. Stimulated optical radiation in ruby. *Nature*, 187(4736):493–494, August 1960.

[5] M. Hentschel, R. Kienberger, C. Spielmann, G. A. Reider, N. Milosevic, T. Brabec, P. Corkum, U. Heinzmann, M. Drescher, and F. Krausz. Attosecond metrology. *Nature*, 414(6863):509–513, November 2001.

[6] P. Baum and A. H. Zewail. Attosecond electron pulses for 4D diffraction and microscopy. *Proceedings of the National Academy of Sciences of the United States of America*, 104(47):18409–18414, November 2007.

[7] R. J. D. Miller, R. Ernstorfer, M. Harb, M. Gao, C. T. Hebeisen, H. Jean-Ruel, C. Lu, G. Moriena, and G. Sciaini. 'Making the molecular movie': first frames. *Acta Crystallographica Section A: Foundations of Crystallography*, 66(2):137–156, March 2010.

[8] R. J. D. Miller. Femtosecond crystallography with ultrabright electrons and x-rays: Capturing chemistry in action. *Science*, 343(6175):1108–1116, March 2014.

[9] C. Bostedt, J. D. Bozek, P. H. Bucksbaum, R. N. Coffee, J. B. Hastings, Z. Huang, R. W. Lee, S. Schorb, J. N. Corlett, P. Denes, P. Emma, R. W. Falcone, et al. Ultra-fast and ultra-intense x-ray sciences: first results from the linac coherent light source free-electron laser. *Journal of Physics B: Atomic, Molecular and Optical Physics*, 46(16):164003, August 2013.

[10] J. Andreasson, A. V. Martin, M. Liang, N. Timneanu, A. Aquila, F. Wang, B. Iwan, M. Svenda, T. Ekeberg, M. Hantke, J. Bielecki, D. Rolles, A. Rudenko, L. Foucar, R. Hartmann, B. Erk, B. Rudek, et al. Automated identification and classification of single particle serial femtosecond x-ray diffraction data. *Opt. Express*, 22(3):2497–2510, February 2014.

[11] H. N. Chapman, P. Fromme, A. Barty, T. A. White, R. A. Kirian, A. Aquila, M. S. Hunter, J. Schulz, D.P. DePonte, U. Weierstall, R. B. Doak, F. R. N. C. Maia, A. V. Martin, I. Schlichting, L. Lomb, et al. Femtosecond x-ray protein nanocrystallography. *Nature*, 470(7332):73–77, February 2011.

[12] A. Barty, C. Caleman, A. Aquila, N. Timneanu, L. Lomb, T. A. White, J. Andreasson, D. Arnlund, S. Bajt, T. R. M. Barends, M. Barthelmess, M. J. Bogan, C. Bostedt, J. D. Bozek, R. Coffee, and et al. Self-terminating diffraction gates femtosecond x-ray nanocrystallography measurements. *Nature Photonics*, 6(1):35–40, January 2012.

[13] T. Tanaka. Proposal for a pulse-compression scheme in x-ray free-electron lasers to generate a multiterawatt, attosecond x-ray pulse. *Phys. Rev. Lett.*, 110:084801, February 2013.

[14] M. Fuchs, R. Weingartner, A. Popp, Z. Major, S. Becker, J. Osterhoff, I. Cortrie, B. Zeitler, R. Horlein, G. D. Tsakiris, U. Schramm, T. P. Rowlands-Rees, S. M. Hooker, D. Habs, F. Krausz, S. Karsch, and F. Grüner. Laser-driven soft-x-ray undulator source. *Nature Physics*, 5(11):826–829, November 2009.

[15] A. Buck, M. Nicolai, K. Schmid, C. M. S. Sears, A. Savert, J. M. Mikhailova, F. Krausz, M. C. Kaluza, and L. Veisz. Real-time observation of laser-driven electron acceleration. *Nature Physics*, 7(7):543–548, July 2011.

[16] A. R. Maier, A. Meseck, S. Reiche, C. B. Schroeder, T. Seggebrock, and F. Grüner. Demonstration scheme for a laser-plasma-driven free-electron laser. *Phys. Rev. X*, 2:031019, September 2012.

[17] F. Grüner, S. Becker, U. Schramm, T. Eichner, M. Fuchs, R. Weingartner, D. Habs, J. Meyer-ter Vehn, M. Geissler, M. Ferrario, L. Serafini, B. van der Geer, H. Backe, W. Lauth, and S. Reiche. Design considerations for table-top, laser-based vuv and x-ray free electron lasers. *Applied Physics B*, 86(3):431–435, January 2007.

[18] K. Nakajima. Compact x-ray sources: Towards a table-top free-electron laser. *Nat Phys*, 4(2):92–93, February 2008.

[19] M. Chergui and A. H. Zewail. Electron and x-ray methods of ultrafast structural dynamics: Advances and applications. *ChemPhysChem*, 10(1):28–43, January 2009.

[20] T. van Oudheusden. *Electron source for sub-relativistic single-shot femtosecond diffraction*. PhD thesis, TuEindhoven, 2010.

[21] M. Aidelsburger, F. O. Kirchner, F. Krausz, and P. Baum. Single-electron pulses for ultrafast diffraction. *Proceedings of the National Academy of Sciences of the United States of America*, 107(46):19714–19719, November 2010.

[22] V. A. Lobastov, R. Srinivasan, and A. H. Zewail. Four-dimensional ultrafast electron microscopy. *Proceedings of the National Academy of Sciences of the United States of America*, 102(20):7069–7073, May 2005.

[23] S. Lahme, C. Kealhofer, F. Krausz, and P. Baum. Femtosecond single-electron diffraction. *Structural Dynamics*, 1(3):034303, June 2014.

[24] S. Lahme. *Femtosecond single-electron diffraction*. PhD thesis, LMU, 2014.

[25] F. O. Kirchner. *Ultrashort and coherent single-electron pulses for diffraction at ultimate resolutions*. PhD thesis, LMU, 2013.

[26] A. Gliserin, A. Apolonski, F. Krausz, and P. Baum. Compression of single-electron pulses with a microwave cavity. *New Journal of Physics*, 14:073055, July 2012.

[27] P. Baum, D. S. Yang, and A. H. Zewail. 4D visualization of transitional structures in phase transformations by electron diffraction. *Science*, 318(5851):788–792, November 2007.

[28] E. Fill, L. Veisz, A. Apolonski, and F. Krausz. Sub-fs electron pulses for ultrafast electron diffraction. *New Journal of Physics*, 8:272, November 2006.

[29] L. Veisz, G. Kurkin, K. Chernov, V. Tarnetsky, A. Apolonski, F. Krausz, and E. Fill. Hybrid DC-AC electron gun for fs-electron pulse generation. *New Journal of Physics*, 9:451, December 2007.

[30] P. Hansen, C. Baumgarten, H. Batelaan, and M. Centurion. Dispersion compensation for attosecond electron pulses. *Applied Physics Letters*, 101(8):083501, August 2012.

[31] S. Lahme, A. Gliserin, M. Walbran, F. Krausz, and P. Baum. Ten-femtosecond (rms) single-electron diffraction. In *19th International Conference on Ultrafast Phenomena*, page 09.Wed.C.1. Optical Society of America, 2014.

[32] A. Gliserin. *Towards attosecond 4D imaging of atomic-scale dynamics by single-electron diffraction.* PhD thesis, LMU, 2014.

[33] P. Baum. On the physics of ultrashort single-electron pulses for time-resolved microscopy and diffraction. *Chemical Physics*, 423:55–61, September 2013.

[34] J. C. Vickerman and I. S. Gilmore. *Surface analysis: the principal techniques*, volume 2. Wiley Online Library, 2009.

[35] Müller BBM. Aktive Magnetfeldkompensationsanlage. *http://www.muellerbbm.de/produkte/aktive-magnetfeldkompensation/*, [online accessed December 01, 2014].

[36] W. Schneider, A. Ryabov, Cs. Lombosi, T. Metzger, Zs. Major, J. A. Fülöp, and P. Baum. 800-fs, 330-μJ pulses from a 100-W regenerative Yb:YAG thin-disk amplifier at 300 kHz, and THz generation in LiNbO3. *Optics Letters, in print (Dec 2014)*, 2014.

[37] L. L. Alston. *High-voltage technology.* Oxford university press, 1986.

[38] British Geological Survey. World magnetic model. *http://www.geomag.bgs.ac.uk/data_service/models_compass/wmm_calc.htmlf*, [online accessed March 27, 2011].

[39] M. Beyer, W. Boeck, K. Möller, and W. Zaengl. Hochspannungstechnik - Theoretische und praktische Grundlagen für die Anwendung. *Springer-Verlag*, 1986.

[40] F. Paschen. Über die zum Funkenübergang in Luft, Wasserstoff und Kohlensäure bei verschiedenen Drucken erforderliche Potentialdifferenz. *Ann. Phys.*, 273:69–96, 1889.

[41] H.C. Miller. Surface flashover of insulators. *Electrical Insulation, IEEE Transactions*, 24(5):765–786, 1989.

[42] A. Roth. *Hochspannungstechnik*. Springer-Verlag, 1965.

[43] P. Baum. Towards ultimate temporal and spatial resolutions with ultrafast single-electron diffraction. *Journal of Physics B-atomic Molecular and Optical Physics*, 47(12):124005, June 2014.

[44] J. Moore, C. Davis, M. Coplan, and S. Greer. *Building scientific apparatus*. Cambridge university press, 2009.

[45] Ensinger Sintimid. Materialdatenblatt, 2009. *http://www.ensinger-online.com/fileadmin/pictures-pdf/General_informations/Technical_Informations/TECASINT-datasheets/Deutsch/TECASINT-2011-deutsch.pdf*, [online accessed September 18, 2014].

[46] *Heinzinger electronic GmbH. Heinzinger® PNChp+150000-1 neg Datenblatt*, 2011.

[47] *Tietz Video and Image Processing Systems GmbH. Datenblatt TemCam-F416*, 2011.

[48] T. Urban. Charakterisierung und Optimierung der Detektion von Einzelelektronen für die ultraschnelle Elektronenbeugung. *Bachelor thesis, TU München*, 2014.

[49] S. U. Ay, M. P. Lesser, and E. R. Fossum. CMOS Active Pixel Sensor (APS) imager for scientific applications. *Survey and Other Telescope Technologies and Discoveries*, 4836:271, December 2002.

[50] P. Dorenbos, J. T. M. de Haas, and C. W. E. Van Eijk. Non-proportionality in the scintillation response and the energy resolution obtainable with scintillation crystals. *IEEE Transactions on Nuclear Science*, 42(6):2190–2202, December 1995.

[51] W. W. Moses, S. A. Payne, W. S. Choong, G. Hull, and B. W. Reutter. Scintillator non-proportionality: Present understanding and future challenges. *IEEE Transactions on Nuclear Science*, 55(3):1049–1053, June 2008.

[52] W. W. Moses, G. A. Bizarri, R. T. Williams, S. A. Payne, A. N. Vasil'ev, J. Singh, Q. Li, J. Q. Grim, and W. Choong. The origins of scintillator non-proportionality. *IEEE Transactions on Nuclear Science*, 59(5):2038–2044, October 2012.

[53] S. Humphries. *Principles of Charged Particle Acceleration*. Wiley-Interscience, 1st edition, March 1986.

[54] L. Bergmann and C. Schäfer. *Lehrbuch der Experimentalphysik - Band III Optik*. Springer Verlag, 6th edition, 1974.

[55] H. Zijlstra. *Experimental methods in magnetism, 1. generation and computation of magnetic fields*. North Holland Publishing Co., 1967.

[56] D. Kreier, D. Sabonis, and P. Baum. Alignment of magnetic solenoid lenses for minimizing temporal distortions. *Journal of Optics*, 16(7):075201, July 2014.

[57] M. Haider, S. Uhlemann, E. Schwan, H. Rose, B. Kabius, and K. Urban. Electron microscopy image enhanced. *Nature*, 392(6678):768–769, April 1998.

[58] D. J. Flannigan and A. H. Zewail. 4D electron microscopy: Principles and applications. *Accounts of Chemical Research*, 45(10):1828–1839, November 2012.

[59] G. Sciaini and R. J. D. Miller. Femtosecond electron diffraction: heralding the era of atomically resolved dynamics. *Reports On Progress In Physics*, 74(9):096101, September 2011.

[60] C. Weninger and P. Baum. Temporal distortions in magnetic lenses. *Ultramicroscopy*, 113:145–151, February 2012.

[61] F. O. Kirchner, S. Lahme, F. Krausz, and P. Baum. Coherence of femtosecond single electrons exceeds biomolecular dimensions. *New Journal of Physics*, 15(6):063021, June 2013.

[62] S. B. van der Geer, M. J. de Loos, E. J. D. Vredenbregt, and O. J. Luiten. Ultracold electron source for single-shot, ultrafast electron diffraction. *Microscopy and Microanalysis*, 15(4):282–289, August 2009.

[63] W. J. Engelen, M. A. van der Heijden, D. J. Bakker, E. J. D. Vredenbregt, and O. J. Luiten. High-coherence electron bunches produced by femtosecond photoionization. *Nature Communications*, 4:1693, April 2013.

[64] A. J. McCulloch, D. V. Sheludko, M. Junker, and R. E. Scholten. High-coherence picosecond electron bunches from cold atoms. *Nature Communications*, 4:1692, April 2013.

[65] A. Paarmann, M. Gulde, M. Mueller, S. Schaefer, S. Schweda, M. Maiti, C. Xu, T. Hohage, F. Schenk, C. Ropers, and R. Ernstorfer. Coherent femtosecond low-energy single-electron pulses for time-resolved diffraction and imaging: A numerical study. *Journal of Applied Physics*, 112(11):113109, December 2012.

[66] J. Hoffrogge, J. P. Stein, M. Krüger, M. Förster, J. Hammer, D. Ehberger, P.r Baum, and P. Hommelhoff. Tip-based source of femtosecond electron pulses at 30 keV. *Journal of Applied Physics*, 115(9):094506, March 2014.

[67] A. H. Zewail. Four-dimensional electron microscopy. *Science*, 328(5975):187–193, April 2010.

[68] F. O. Kirchner, A. Gliserin, F. Krausz, and P. Baum. Laser streaking of free electrons at 25 keV. *Nature Photonics*, 8(1):52–57, January 2014.

[69] P. Baum and A. H. Zewail. 4D attosecond imaging with free electrons: Diffraction methods and potential applications. *Chemical Physics*, 366(1-3):2–8, December 2009.

[70] W. Bühring, H. Rebel, and G. Schatz. Method for alignment of a short magnetic lens beta-ray spectrometer by utilizing image rotation. *Nuclear Instruments & Methods*, 26(2):267–268, February 1964.

[71] T. van Oudheusden, P. L. E. M. Pasmans, S. B. van der Geer, M. J. de Loos, M. J. van der Wiel, and O. J. Luiten. Compression of subrelativistic space-charge-dominated electron bunches for single-shot femtosecond electron diffraction. *Physical Review Letters*, 105(26):264801, December 2010.

[72] M. Gao, H. Jean-Ruel, R. R. Cooney, J. Stampe, M. de Jong, M. Harb, G. Sciaini, G. Moriena, and R. J. D. Miller. Full characterization of rf compressed femtosecond electron pulses using ponderomotive scattering. *Optics Express*, 20(11):12048–12058, May 2012.

[73] R. P. Chatelain, V. R. Morrison, C. Godbout, and B. J. Siwick. Ultrafast electron diffraction with radio-frequency compressed electron pulses. *Applied Physics Letters*, 101(8):081901, August 2012.

[74] P. L. E. M. Pasmans, G. B. van den Ham, S. F. P. Dal Conte, S. B. van der Geer, and O. J. Luiten. Microwave TM010 cavities as versatile 4D electron optical elements. *Ultramicroscopy*, 127:19–24, April 2013.

[75] K. Jung and J. Kim. Subfemtosecond synchronization of microwave oscillators with mode-locked er-fiber lasers. *Optics Letters*, 37(14):2958–2960, July 2012.

[76] A. Gliserin, M. Walbran, and P. Baum. Passive optical enhancement of laser-microwave synchronization. *Applied Physics Letters*, 103(3):031113, July 2013.

[77] P. Dombi, P. Rácz, L. Veisz, and P. Baum. Conversion of chirp in fiber compression. *Optics Letters*, 39(8):2232–2235, April 2014.

[78] D. Kreier and P. Baum. Avoiding temporal distortions in tilted pulses. *Optics Letters*, 37(12):2373–2375, June 2012.

[79] T. Brabec and F. Krausz. Intense few-cycle laser fields: Frontiers of nonlinear optics. *Reviews of Modern Physics*, 72(2):545, April 2000.

[80] L. Kasmi, D. Kreier, M. Bradler, E. Riedle, and P. Baum. Femtosecond single-electron pulses generated by two-photon photoemission close to the work function. *submitted to New J. Phys.*, 2015.

[81] L. Kasmi. Tunable femtosecond NOPA pulses for single-electron generation by two-photon photoemission. *Master thesis, LMU München and Swiss Federal Institute of Technology of Lausanne*, September 2013.

[82] D. Shorokhov and A. H. Zewail. 4D electron imaging: principles and perspectives. *Physical Chemistry Chemical Physics*, 10(20):2879–2893, 2008.

[83] M. Eichberger, H. Schafer, M. Krumova, M. Beyer, J. Demsar, H. Berger, G. Moriena, G. Sciaini, and R. J. D. Miller. Snapshots of cooperative atomic motions in the optical suppression of charge density waves. *Nature*, 468(7325):799–802, December 2010.

[84] Haihua Liu, Oh-Hoon Kwon, Jau Tang, and Ahmed H. Zewail. 4D imaging and diffraction dynamics of single-particle phase transition in heterogeneous ensembles. *Nano Letters*, 14(2):946–954, January 2014.

[85] V. R. Morrison, R. P. Chatelain, K. L. Tiwari, A. Hendaoui, A. Bruhács, M. Chaker, and B. J. Siwick. A photoinduced metal-like phase of monoclinic VO2 revealed by ultrafast electron diffraction. *Science*, 346(6208):445–448, October 2014.

[86] H. Ihee, V. A. Lobastov, U. M. Gomez, B. M. Goodson, R. Srinivasan, C. Y. Ruan, and A. H. Zewail. Direct imaging of transient molecular structures with ultrafast diffraction. *Science*, 291(5503):458–462, January 2001.

[87] R. Srinivasan, J. S. Feenstra, S. T. Park, S. J. Xu, and A. H. Zewail. Dark structures in molecular radiationless transitions determined by ultrafast diffraction. *Science*, 307(5709):558–563, January 2005.

[88] C. J. Hensley, J. Yang, and M. Centurion. Imaging of isolated molecules with ultrafast electron pulses. *Physical Review Letters*, 109(13):133202, September 2012.

[89] M. Gao, C. Lu, H. Jean-Ruel, L. C. Liu, A. Marx, K. Onda, S. Koshihara, Y. Nakano, X. Shao, T. Hiramatsu, G. Saito, H. Yamochi, R. R. Cooney, G. Moriena, G. Sciaini, and R. J. D. Miller. Mapping molecular motions leading to charge delocalization with ultrabright electrons. *Nature*, 496(7445):343–346, April 2013.

[90] S. Wall, B. Krenzer, S. Wippermann, S. Sanna, F. Klasing, A. Hanisch-Blicharski, M. Kammler, W. G. Schmidt, and M. Horn-von Hoegen. Atomistic picture of charge density wave formation at surfaces. *Physical Review Letters*, 109(18):186101, November 2012.

[91] S. T. Park, A. Yurtsever, J. S. Baskin, and A. H. Zewail. Graphene-layered steps and their fields visualized by 4D electron microscopy. *Proceedings of the National Academy of Sciences of the United States of America*, 110(23):9277–9282, June 2013.

[92] B. J. Siwick, J. R. Dwyer, R. E. Jordan, and R. J. D. Miller. Ultrafast electron optics: Propagation dynamics of femtosecond electron packets. *Journal of Applied Physics*, 92(3):1643–1648, August 2002.

[93] G. H. Kassier, N. Erasmus, K. Haupt, I. Boshoff, R. Siegmund, S. M. M. Coelho, and H. Schwoerer. Photo-triggered pulsed cavity compressor for bright electron bunches in ultrafast electron diffraction. *Applied Physics B-lasers and Optics*, 109(2):249–257, November 2012.

[94] C. M. Scoby, R. K. Li, E. Threlkeld, H. To, and P. Musumeci. Single-shot 35 fs temporal resolution electron shadowgraphy. *Applied Physics Letters*, 102(2):023506, January 2013.

[95] W. E. Spicer. Optical transitions in which crystal momentum is not conserved. *Physical Review Letters*, 11(6):243–&, July 1963.

[96] W. E. Spicer. Possible non-one-electron effects in fundamental optical excitation spectra of certain crystalline solids and their effect on photoemission. *Physical Review*, 154(2):385–&, May 1967.

[97] I. Z. Kozma, P. Baum, S. Lochbrunner, and E. Riedle. Widely tunable sub-30 fs ultraviolet pulses by chirped sum frequency mixing. *Optics Express*, 11(23):3110–3115, November 2003.

[98] P. Baum, S. Lochbrunner, and E. Riedle. Tunable sub-10-fs ultraviolet pulses generated by achromatic frequency doubling. *Optics letters*, 29(14):1686–1688, July 2004.

[99] M. Bradler and E. Riedle. Sub-20 fs μJ-energy pulses tunable down to the near-UV from a 1 MHz Yb-fiber laser system. *Optics Letters*, 39(9):2588–2591, May 2014.

[100] C. T. Hebeisen, R. Ernstorfer, M. Harb, T. Dartigalongue, R. E. Jordan, and R. J. D. Miller. Femtosecond electron pulse characterization using laser ponderomotive scattering. *Optics Letters*, 31(23):3517–3519, December 2006.

[101] C. T. Hebeisen, G. Sciaini, M. Harb, R. Ernstorfer, T. Dartigalongue, S. G. Kruglik, and R. J. D. Miller. Grating enhanced ponderomotive scattering for visualization and full characterization of femtosecond electron pulses. *Optics Express*, 16(5):3334–3341, March 2008.

[102] D. Wytrykus, M. Centurion, P. Reckenthaeler, F. Krausz, A. Apolonski, and E. Fill. Ultrashort pulse electron gun with a MHz repetition rate. *Applied Physics B-lasers and Optics*, 96(2-3):309–314, August 2009.

[103] D.-S. Yang, O. F. Mohammed, and A. H. Zewail. Scanning ultrafast electron microscopy. *Proceedings of the National Academy of Sciences of the United States of America*, 107(34):14993–14998, August 2010.

[104] C. Homann, C. Schriever, P. Baum, and E. Riedle. Octave wide tunable UV-pumped NOPA: pulses down to 20 fs at 0.5 MHz repetition rate. *Optics Express*, 16(8):5746–5756, April 2008.

[105] M. Bradler, P. Baum, and E. Riedle. Femtosecond continuum generation in bulk laser host materials with sub-μJ pump pulses. *Applied Physics B-lasers and Optics*, 97(3):561–574, November 2009.

[106] R. Riedel, A. Stephanides, M. J. Prandolini, B. Gronloh, B. Jungbluth, T. Mans, and F. Tavella. Power scaling of supercontinuum seeded megahertz-repetition rate optical parametric chirped pulse amplifiers. *Optics Letters*, 39(6):1422–1424, March 2014.

[107] I. Z. Kozma, P. Baum, U. Schmidhammer, S. Lochbrunner, and E. Riedle. Compact autocorrelator for the online measurement of tunable 10 femtosecond pulses. *Review of Scientific Instruments*, 75(7):2323–2327, July 2004.

[108] K. L. Jensen, P. G. O'Shea, D. W. Feldman, and N. A. Moody. Theoretical model of the intrinsic emittance of a photocathode. *Applied Physics Letters*, 89(22):224103, November 2006.

[109] Vision Dimension. DHHV3151UC-ML Datenblatt. *http://www.vd-shop.de/usbcolor-high-resolution-minicamera-dhhv3151ucml-p-293.html*, [online accessed November 27, 2014].

[110] J. C. Williamson and A. H. Zewail. Ultrafast electron diffraction. Velocity mismatch and temporal resolution in crossed-beam experiments. *Chemical Physics Letters*, 209(1-2):10–16, June 1993.

[111] P. Baum and A. H. Zewail. Breaking resolution limits in ultrafast electron diffraction and microscopy. *Proceedings of the National Academy of Sciences of the United States of America*, 103(44):16105–16110, October 2006.

[112] H. Daido. Review of soft x-ray laser researches and developments. *Reports on Progress in Physics*, 65(10):1513, 2002.

[113] R. Tommasini and E. E. Fill. Effective traveling-wave excitation below the speed of light. *Optics Letters*, 26(10):689–691, May 2001.

[114] T. Kobayashi and A. Shirakawa. Tunable visible and near-infrared pulse generator in a 5Â fs regime. *Appl. Phys. B*, 70(S1):239–246, June 2000.

[115] A. Stepanov, J. Kuhl, I. Kozma, E. Riedle, G. Almási, and J. Hebling. Scaling up the energy of thz pulses created by optical rectification. *Optics express*, 13(15):5762–5768, July 2005.

[116] J. Hebling, K. Yeh, M. C. Hoffmann, B. Bartal, and K. Nelson. Generation of high-power terahertz pulses by tilted-pulse-front excitation and their application possibilities. *JOSA B*, 25(7):B6–B19, July 2008.

[117] K. Tanaka, H. Hirori, and M. Nagai. Thz nonlinear spectroscopy of solids. *IEEE Trans. Terahertz Sci. Technol*, 1(1):301–312, 2011.

[118] M. C. Hoffmann and J. A. Fülöp. Intense ultrashort terahertz pulses: generation and applications. *Journal of Physics D: Applied Physics*, 44(8):083001 (17pp), 2011.

[119] Z. Bor and B. Racz. Group velocity dispersion in prisms and its application to pulse compression and travelling-wave excitation. *Optics communications*, 54(3):165–170, June 1985.

[120] O. E. Martinez. Grating and prism compressors in the case of finite beam size. *JOSA B*, 3(7):929–934, July 1986.

[121] J. Hebling. Derivation of the pulse front tilt caused by angular dispersion. *Optical and Quantum Electronics*, 28(12):1759–1763, July 1996.

[122] L. Pálfalvi, J. A. Fülöp, G. Almási, and J. Hebling. Novel setups for extremely high power single-cycle terahertz pulse generation by optical rectification. *Applied Physics Letters*, 92(17):171107–171107, 2008.

[123] J. A. Fülöp, L. Pálfalvi, G. Almási, and J. Hebling. Design of high-energy terahertz sources based on optical rectification. *Optics express*, 18(12):12311–12327, June 2010.

[124] J.-C. Chanteloup, E. Salmon, C. Sauteret, A. Migus, P. Zeitoun, A. Klisnick, A. Carillon, S. Hubert, D. Ros, P. Nickles, and M. Kalachnikov. Pulse-front control of 15-tw pulses with a tilted compressor, and application to the subpicosecond traveling-wave pumping of a soft-x-ray laser. *JOSA B*, 17(1):151–157, January 2000.

[125] J. A. Fülöp, L. Pálfalvi, S. Klingebiel, G. Almási, F. Krausz, S. Karsch, and J. Hebling. Generation of sub-mj terahertz pulses by optical rectification. *Optics letters*, 37(4):557–559, February 2012.

[126] Z. Major, S. A. Trushin, I. Ahmad, M. Siebold, C. Wandt, S. Klingebiel, T.-J. Wang, J. A. Fülöp, A. Henig, S. Kruber, R. Weingartner, A. Popp, J. Osterhoff, R. Hörlein, J. Hein, V. Pervak, A. Apolonski, F. Krausz, and S. Karsch. Basic concepts and current status of the petawatt field synthesizer - a new approach to ultrahigh field generation. *Rev. Laser Engineering*, 37:431–436, 2009.

[127] T. Ganz, V. Pervak, A. Apolonski, and P. Baum. 16 fs, 350 nJ pulses at 5 MHz repetition rate delivered by chirped pulse compression in fibers. *Optics Letters*, 36(7):1107–1109, April 2011.

[128] S. T. Park, D. J. Flannigan, and A. H. Zewail. 4D electron microscopy visualization of anisotropic atomic motions in carbon nanotubes. *Journal of the American Chemical Society*, 134(22):9146–9149, May 2012.

[129] S. Iijima. Helical microtubules of graphitic carbon. *Nature*, 354(6348):56–58, November 1991.

[130] A. Maeda, S. Matsumoto, H. Kishida, T. Takenobu, Y. Iwasa, M. Shiraishi, M. Ata, and H. Okamoto. Large optical nonlinearity of semiconducting single-walled carbon nanotubes under resonant excitations. *Phys. Rev. Lett.*, 94:047404, February 2005.

[131] P. Avouris, M. Freitag, and V. Perebeinos. Carbon-nanotube photonics and optoelectronics. *Nature Photonics*, 2(6):341–350, June 2008.

[132] L. Yong-Bing, S. Li, Z. Chun-Yu, W. Li, F. Pan-Ming, Z. Zhi-Guo, X. Si-Shen, and W. Guo-Ping. Ultrafast carrier dynamics in purified and as-grown single-walled carbon nanotube films. *Chinese Physics*, 14(10):2137, October 2005.

[133] M.-F. Yu, O. Lourie, M. J. Dyer, K. Moloni, T. F. Kelly, and R. S. Ruoff. Strength and breaking mechanism of multiwalled carbon nanotubes under tensile load. *Science*, 287(5453):637–640, January 2000.

[134] T. W. Ebbesen, H. J. Lezec, H. Hiura, J. W. Bennett, H. F. Ghaemi, and T. Thio. Electrical conductivity of individual carbon nanotubes. *Nature*, 382(6586):54–56, July 1996.

[135] S. Berber, Y.-K. Kwon, and D. Tomanek. Unusually high thermal conductivity of carbon nanotubes. *Phys. Rev. Lett.*, 84(20):4613, May 2000.

[136] W. A. deHeer, W. S. Bacsa, A. Châtelain, T. Gerfin, R. Humphrey-Baker, L. Forro, and D. Ugarte. Aligned carbon nanotube films: Production and optical and electronic properties. *Science*, 268(5212):845–847, May 1995.

[137] A. Gambetta, E. Manzoni, C.and Menna, M. Meneghetti, G. Cerullo, G. Lanzani, S. Tretiak, A. Piryatinski, A. Saxena, R. L. Martin, and A. R. Bishop. Real-time observation of nonlinear coherent phonon dynamics in single-walled carbon nanotubes. *Nature Physics*, 2(8):515–520, July 2006.

[138] R. H. Baughman. Putting a new spin on carbon nanotubes. *Science*, 290(5495):1310–1311, 2000.

[139] N. Behabtu, C. C. Young, D. E. Tsentalovich, O. Kleinerman, X. Wang, A. W. Ma, E. A. Bengio, R. F. ter Waarbeek, J. J. de Jong, R. E. Hoogerwerf, S. B. Fairchild, J. B. Ferguson, B. Maruyama, J. Kono, Y. Talmon, Y. Cohen, M. J. Otto, and M. Pasquali. Strong, light, multifunctional fibers of carbon nanotubes with ultrahigh conductivity. *Science*, 339(6116):182–186, January 2013.

[140] Y. Zhou, A. Gaur, S.-H. Hur, C. Kocabas, M. A. Meitl, M. Shim, and J. A. Rogers. p-channel, n-channel thin film transistors and p-n diodes based on single wall carbon nanotube networks. *Nano Letters*, 4(10):2031–2035, August 2004.

[141] S.-L. Chen, Y.-C. Chang, C. Zhang, J. G. Ok, T. Ling, M. T. Mihnev, T. B. Norris, and L. J. Guo. Efficient real-time detection of terahertz pulse radiation based on photoacoustic conversion by carbon nanotube nanocomposite. *Nature Photonics*, 8(7):537–542, July 2014.

[142] E. S. Snow, F. K. Perkins, E. J. Houser, S. C. Badescu, and T. L. Reinecke. Chemical detection with a single-walled carbon nanotube capacitor. *Science*, 307(5717):1942–1945, March 2005.

[143] M. M. Shulaker, G. Hills, N. Patil, H. Wei, H. Chen, H.-S. P. Wong, and S. Mitra. Carbon nanotube computer. *Nature*, 501(7468):526–530, September 2013.

[144] B. C. Edwards. Design an deployment of a space elevator. *Acta Astronautica*, 47(10):735 – 744, November 2000.

[145] T. Hertel, R. Fasel, and G. Moos. Charge-carrier dynamics in single-wall carbon nanotube bundles: a time-domain study. *Applied Physics A*, 75(4):449–465, October 2002.

[146] M. S. Dresselhaus, G. Dresselhaus, R. Saito, and A. Jorio. Raman spectroscopy of carbon nanotubes. *Physics Reports*, 409(2):47–99, March 2005.

[147] W. Ma, L. Song, R. Yang, T. Zhang, Y. Zhao, L. Sun, Y. Ren, D. Liu, L. Liu, J. Shen, Z. Zhang, Y. Xiang, W. Zhou, and S. Xie. Directly synthesized strong, highly conducting, transparent single-walled carbon nanotube films. *Nano Letters*, 7(8):2307–2311, July 2007. PMID: 17629347.

[148] plano GmbH. Dünnstegnetzchen. *http://www.cp-download.de/plano11/Kapitel-1.pdf*, [online accessed December 08, 2014].

[149] PI miCos GmbH. Linear Stage LS 110. *http://www.pimicos.com/web2/en/1,4,110,ls110.html*, [online accessed December 02, 2014].

[150] L.-C. Qin. Electron diffraction from carbon nanotubes. *Reports on Progress in Physics*, 69(10):2761, September 2006.

[151] T. Yamabe, K. Fukui, and K. Tanaka. *The science and technology of carbon nanotubes*. Elsevier, 1999.

[152] A. A. Lucas, V. Bruyninckx, P. Lambin, D. Bernaerts, S. Amelinckx, J. V. Landuyt, and G. V. Tendeloo. Electron diffraction by carbon nanotubes. *Scanning Microscopy*, 12(3):415–436, 1998.

[153] F. Carbone, P. Baum, P. Rudolf, and A. H. Zewail. Structural preablation dynamics of graphite observed by ultrafast electron crystallography. *Physical Review Letters*, 100(3):035501, January 2008.

[154] R. K. Raman, Y. Murooka, C.-Y. Ruan, T. Yang, S. Berber, and D. Tománek. Direct observation of optically induced transient structures in graphite using ultrafast electron crystallography. *Phys. Rev. Lett.*, 101:077401, August 2008.

[155] S. Schäfer, W. Liang, and A. H. Zewail. Primary structural dynamics in graphite. *New Journal of Physics*, 13(6):063030, June 2011.

Data archiving

All original figures, experimental raw-data, evaluation and simulation tools are stored on the Data Archive Server of the Laboratory for Attosecond Physics at the Max Planck Institute of Quantum Optics: /afs/rzg/mpq/lap/publication_archive

The data is organized with respect to the chapters and sub-chapters in the thesis. All original figures are named *figXX-XX-text* with *XX-XX* the number as in the thesis and *-text* a short description of the figure similar to the figure name. The editable figures and the corresponding evaluations or simulations are also provided and the file-names or folders have the same number *XX-XX* as the figure. Some evaluation tools are used to generate more than one figure and are stored in the main folder (.../evaluation tools). Supplementary information can be found in text files, providing, if applicable, descriptions about data acquisition, processing, evaluation or simulation.

Acknowledgment

At this point I would like to thank all who contributed to the success of this work. Without you, this work would not have been possible. My special thanks go to

- Prof. Dr. Ferenc Krausz for the support and the confidence placed in me in awarding this thesis.
- Prof. Dr. Jochen Feldmann who has kindly agreed to review my thesis.
- Dr. Peter Baum for his guidance and help in many things during this project. Especially I want to thank you for never stopping motivating me in the beginning of this work, when I spent plenty of time in endless tedious "Bauamt"-discussions to establish the new laboratory.
- Rolf Öhm and his team at the mechanical workshop.
- Waldemar Schneider and Andrey Ryabanov for the great collaboration in the laboratory.
- Maximilian Bradler and Lamia Kasmi for helping building up the NOPA.
- My office mates Olga Razskazovskaya, Dr. Ivan Angelov and Simon Holzberger who had to endure sometimes very long telephone calls I had with different companies to bargain about several equipment. There were times when the place looked more like a "goods receiving department" than like an office.
- Dr. Alexander Gliserin for support in programming with Labview.
- Dr. Stefan Lahme and Dr. Friedrich Kirchner for many scientific discussions and advices.
- Dagmar Frischke for support with coating the photo-cathodes.

- Dr. Wenjun Ma for providing the carbon nanotube foils.
- Dr. Johannes Wulz for helping with technical drawings.
- the UED-team for the good working atmosphere.
- my girlfriend Johanna, my family and my friends for moral support and much more.